A spatial windowing technique to account for finite dimensions in 2.5D dynamic soil–structure interaction problems

P. Coulier*, A. Dijckmans, S. François, G. Degrande, G. Lombaert

KU Leuven, Department of Civil Engineering, Kasteelpark Arenberg 40, B-3001 Leuven, Belgium

Abstract

The dynamic interaction between a layered halfspace and quasi translationally invariant structures such as roads, railway tracks, tunnels, dams, and lifelines can be modelled using a computationally efficient 2.5D approach, assuming invariance of the geometry in the longitudinal direction. This assumption is not always fulfilled in practice, however. Even for elongated structures, full 3D computations may be required for an accurate solution of the dynamic soil–structure interaction problem. This paper presents a spatial windowing technique for elastodynamic transmission and radiation problems that allows accounting for the finite length of a structure, still maintaining the computational efficiency of a 2.5D formulation. The proposed technique accounts for the diffraction occurring at the structure's edges, but not for its modal behaviour resulting from reflections of waves at its boundaries. Numerical examples of a barrier for vibration transmission and a surface foundation are discussed to demonstrate the accuracy and applicability of the proposed methodology. Full 3D calculations are performed to provide a rigorous validation for each of these examples. It is demonstrated that the proposed technique is appropriate as long as the response is not dominated by the resonant behaviour of individual modes of the structure.

Keywords: Dynamic soil–structure interaction, elastodynamic wave propagation, 2.5D modelling, coupled finite element – boundary element models.

1. Introduction

The numerical solution of three–dimensional (3D) dynamic soil–structure interaction (SSI) problems is a challenging task, in particular for structures with large dimensions. In order to obtain a substantial reduction of the computational effort, the geometry of the problem is in some cases assumed to be invariant in the longitudinal direction. This allows for the application of an efficient two-and-a-half-dimensional (2.5D) approach, where a Fourier transform of the longitudinal coordinate allows representing the 3D response on a 2D mesh. The assumption seems to be valid for roads, railway tracks, tunnels, dams, vibration isolation screens, lifelines, and alluvial valleys [1].

Many applications of the 2.5D concept can be found in the literature. Gavrić [2, 3] uses 2.5D finite elements (FE) to model thin–walled waveguides, while Stamos and Beskos [4] consider 2.5D boundary elements (BE) to model the seismic response of long lined tunnels embedded in a halfspace. In 2.5D BE formulations, analytical full space Green's functions are commonly used [5]. The discretization of the free surface and the layer interfaces can be avoided, however, by employing Green's functions for a layered halfspace [1]. Coupled FE–BE models allow to model complex geometries with the FE method and to account for the radiation of waves in domains of (semi–)infinite extent with the BE method. 2.5D coupled FE–BE formulations have been presented, among others, by Sheng et al. [6], Andersen and Nielsen [7], and Lombaert et al. [8] for the prediction of railway [6, 7] and road traffic [8] induced vibrations. The efficiency

*Corresponding author. Phone: + 32 16 32 16 75. Fax: + 32 16 32 19 88.
Email address: pieter.coulier@bwk.kuleuven.be (P. Coulier*)

Postprint published in Soil Dynamics and Earthquake Engineering

of coupled FE–BE methods is strongly reduced in the case of embedded structures, however, as the Green's functions have to be evaluated for a large number of source/receiver depths for the assembly of the BE matrices. Alternative numerical solution procedures in a 2.5D framework have therefore been formulated as well, such as a 2.5D finite–infinite element approach proposed by Yang et al. [9, 10] or a 2.5D perfectly matched layer (PML) technique described by François et al. [11].

The assumption of longitudinal invariance adopted in 2.5D models is not always fulfilled, however. For example, the length of a vibration isolation screen in the soil is in practice limited and of the same order of magnitude as the wavelength in the soil in the frequency range of interest. Rigorously accounting for the finite length requires the solution of a full 3D dynamic SSI problem, which is computationally very demanding in terms of memory and CPU requirements. The development of adequate numerical methods such as the fast multipole BE method [12] or BE methods based on hierarchical matrices ($\mathscr{H}$–matrices) [13] enables an efficient solution of such large scale problems, but the associated computation times remain relatively high.

In this paper, a spatial windowing technique for elastodynamic transmission and radiation problems is presented that allows accounting for the finite length of a structure, while still maintaining the computational efficiency of a 2.5D formulation. The spatial windowing technique has been proposed by Villot et al. [14] to include the effect of diffraction associated with the finite size of plane structures on sound transmission and radiation. The basic idea of this approach is to apply a spatial rectangular baffle to the structural velocity wavefield of an infinite structure; the windowed wavefield is subsequently employed to compute the radiated wavefield in the wavenumber domain. As a result, only a limited part of the infinite structure contributes to the sound radiation. This technique is mainly used in vibro–acoustic applications, e.g. for the calculation of the transmission loss of sandwich composite panels [15] or for the investigation of the vibro–acoustic response of finite multilayered structures [16] and orthogonally stiffened plates [17]. Spatial windowing is not well suited for acoustic applications at low frequencies (i.e. when individual modes of the structure dominate the response), as it is unable to account for reflected waves at the boundaries to reproduce the resonant behaviour of the modes [17]. At higher frequencies, however, the response shifts from the resonant to the non–resonant mass–law regime and application of the spatial windowing technique leads to results in good agreement with experiments [14, 16, 17].

The aim of this paper is to investigate whether the spatial windowing technique is suited to account for a structure's finite length in 2.5D dynamic SSI problems, using a coupled FE–BE method. Its application to dynamic SSI problems fundamentally differs from acoustic problems, however, as the resonant behaviour of individual modes is strongly affected by the dynamic interaction between the structure and the soil. The text is organized as follows. Section 2 briefly summarizes the governing equations of 3D and 2.5D coupled FE–BE methods. The spatial windowing technique is subsequently introduced in section 3. Numerical examples are considered in sections 4 and 5 to investigate the applicability of the proposed approach. The examples in section 4 involve barriers for vibration transmission in a homogeneous halfspace, which are structures with a finite length that is relatively large compared to the other dimensions. Application of the 2.5D approach hence seems to be appropriate for these cases. Both an empty and filled wave barrier are investigated to determine the influence of the modal behaviour of the structures on the accuracy of the proposed methodology. In section 5, the validity of the spatial windowing technique is further explored by considering a square surface foundation on the soil, which is a structure that can not at all be regarded as invariant. The importance of dynamic SSI is assessed by comparing a foundation on a horizontally layered halfspace to a foundation on a single layer on bedrock. A rigorous validation of the spatial windowing methodology is provided for each of these examples through full 3D computations based on an efficient coupled FE–$\mathscr{H}$-BE method. Concluding remarks regarding the suitability of the proposed technique are summarized in section 6.

2. Coupled FE–BE methods for dynamic soil–structure interaction

Dynamic SSI problems can be solved by means of a subdomain formulation [18, 19], allowing for the application of different numerical techniques for the soil and the structure. In this paper, finite elements are used to model the structural domain Ω_b, while boundary elements on the soil–structure interface Σ

are employed to model wave propagation in the surrounding soil domain Ω_s (figure 1a). Continuity of displacements and equilibrium of stresses are enforced on the interface Σ between the structure and the soil. In the following, it is assumed that tractions $\hat{\underline{\mathbf{t}}}_\mathrm{b}(\omega)$ are imposed on the boundary $\Gamma_{\mathrm{b}\sigma}$ of Ω_b, while an incident wavefield $\hat{\mathbf{u}}_\mathrm{i}(\omega)$ is present in the soil domain Ω_s. A hat above a variable denotes its representation in the frequency domain.

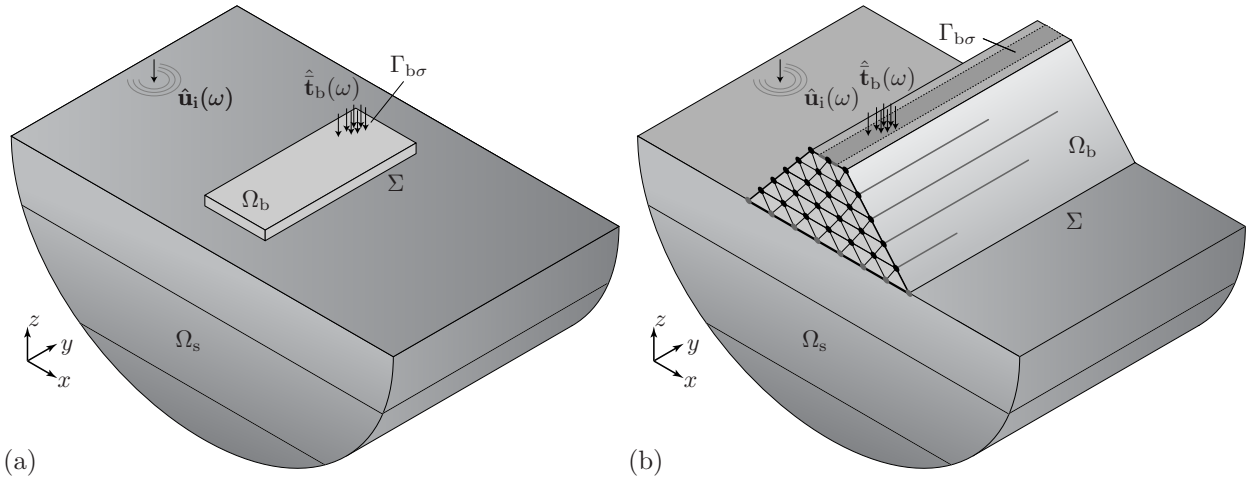

Figure 1: (a) The 3D and (b) the 2.5D dynamic SSI problem, coupling the structural domain Ω_b to the soil domain Ω_s on the soil–structure interface Σ.

2.1. 3D coupled FE–BE method

If a structure with an arbitrary geometry is considered, the rigorous solution of a full 3D dynamic SSI problem is required. A weak variational formulation of the equilibrium of the structure Ω_b results in the following coupled FE–BE equation [18, 20]:

$$\left[\mathbf{K}_\mathrm{b} + \mathbf{C}_\mathrm{b} - \omega^2\mathbf{M}_\mathrm{b} + \widehat{\mathbf{K}}^\mathrm{s}_\mathrm{b}(\omega)\right] \hat{\underline{\mathbf{u}}}_\mathrm{b}(\omega) = \hat{\underline{\mathbf{f}}}_\mathrm{b}(\omega) + \hat{\underline{\mathbf{f}}}^\mathrm{s}_\mathrm{b}(\omega) \tag{1}$$

where $\hat{\underline{\mathbf{u}}}_\mathrm{b}(\omega)$ collects the nodal degrees of freedom of Ω_b, while $\mathbf{K}_\mathrm{b}$, $\mathbf{C}_\mathrm{b}$, and $\mathbf{M}_\mathrm{b}$ are the finite element stiffness, damping, and mass matrices. $\widehat{\mathbf{K}}^\mathrm{s}_\mathrm{b}(\omega)$ is the dynamic soil stiffness matrix and is calculated by means of a 3D BE method. The force vector $\hat{\underline{\mathbf{f}}}_\mathrm{b}(\omega)$ results from tractions $\hat{\underline{\mathbf{t}}}_\mathrm{b}(\omega)$ imposed on the boundary $\Gamma_{\mathrm{b}\sigma}$, whereas $\hat{\underline{\mathbf{f}}}^\mathrm{s}_\mathrm{b}(\omega)$ denotes dynamic SSI forces at the soil–structure interface Σ associated with the incident wavefield $\hat{\mathbf{u}}_\mathrm{i}(\omega)$ [18, 19]. Solving equation (1) provides the structural response $\hat{\underline{\mathbf{u}}}_\mathrm{b}(\omega)$, which corresponds to the soil displacement vector $\hat{\underline{\mathbf{u}}}_\mathrm{s}(\omega)$ on the soil–structure interface Σ due to continuity. The BE equations allow to retrieve the soil tractions $\hat{\underline{\mathbf{t}}}_\mathrm{s}(\omega)$ on Σ:

$$\hat{\underline{\mathbf{t}}}_\mathrm{s}(\omega) = \widehat{\mathbf{U}}^{-1}(\omega)\left(\widehat{\mathbf{T}}(\omega) + \mathbf{I}\right)\hat{\underline{\mathbf{u}}}_\mathrm{s}(\omega) \tag{2}$$

where $\widehat{\mathbf{U}}(\omega)$ and $\widehat{\mathbf{T}}(\omega)$ are BE matrices, requiring integration of the Green's displacements and tractions, respectively. The displacements $\hat{\underline{\mathbf{u}}}_\mathrm{s}(\omega)$ and tractions $\hat{\underline{\mathbf{t}}}_\mathrm{s}(\omega)$ on Σ are subsequently used to evaluate the radiated wavefield $\hat{\underline{\mathbf{u}}}_\mathrm{r}(\omega)$ in the soil through the discretized boundary integral equation:

$$\hat{\underline{\mathbf{u}}}_\mathrm{r}(\omega) = \widehat{\mathbf{U}}_\mathrm{s}(\omega)\hat{\underline{\mathbf{t}}}_\mathrm{s}(\omega) - \widehat{\mathbf{T}}_\mathrm{s}(\omega)\hat{\underline{\mathbf{u}}}_\mathrm{s}(\omega) \tag{3}$$

where $\widehat{\mathbf{U}}_\mathrm{s}(\omega)$ and $\widehat{\mathbf{T}}_\mathrm{s}(\omega)$ are BE transfer matrices.

3D FE–BE models can be used to solve dynamic SSI problems of any size as long as the proper computational resources are available. The fully populated unsymmetric matrices $\widehat{\mathbf{U}}(\omega)$ and $\widehat{\mathbf{T}}(\omega)$ arising from

classical BE formulations lead to stringent memory and CPU requirements, however, restricting the applicability of the method to problems of moderate size. These drawbacks can be circumvented through the application of fast BE methods [12, 13]. In this paper, a fast BE method based on $\mathscr{H}$–matrices [21] is employed for the solution of 3D problems; the reader is referred to the literature [13, 22, 23] for a comprehensive overview of this methodology. The application of $\mathscr{H}$–matrices renders the conventional FE–BE coupling strategy of equation (1) less efficient, however, as it requires the assembly of a dynamic soil stiffness matrix [24]. An alternative iterative Neumann–Dirichlet algorithm is therefore employed, in which the governing equations of the FE and BE subdomain are solved separately, while the boundary conditions at the soil–structure interface are updated until convergence is achieved. A detailed description of this coupling approach can be found in [24].

Although the application of fast BE methods allows increasing the problem size considerably compared to classical BE formulations, the solution of large scale problems remains computationally very demanding. Additional assumptions can be made to simplify the problem, as will be discussed in the next subsection.

2.2. 2.5D coupled FE–BE method

In the case of structures with a longitudinally invariant geometry (figure 1b), the longitudinal coordinate y can be transformed to the wavenumber k_y by means of a forward Fourier transform $\mathscr{F}\left[f(y), k_y\right] = \int_{-\infty}^{+\infty} f(y) \exp\left(ik_y y\right) \mathrm{d}y$, resulting in a computationally efficient 2.5D solution procedure in the frequency–wavenumber domain. As the 3D response can hence be represented on a 2D mesh [1], a substantial reduction of the number of degrees of freedom (and the associated matrix dimensions) is achieved. The governing equations are briefly summarized in this subsection; an extensive discussion of the 2.5D coupled FE–BE methodology can be found in [1, 25].

The dynamic equilibrium equation of the coupled FE–BE system reads as follows in the frequency–wavenumber domain [1]:

$$\left[\tilde{\mathbf{K}}_{\mathrm{b}}(k_y,\omega) + \mathbf{C}_{\mathrm{b}} - \omega^2\mathbf{M}_{\mathrm{b}} + \tilde{\mathbf{K}}^{\mathrm{s}}_{\mathrm{b}}(k_y,\omega)\right] \underline{\tilde{\mathbf{u}}}_{\mathrm{b}}(k_y,\omega) = \underline{\tilde{\mathbf{f}}}_{\mathrm{b}}(k_y,\omega) + \underline{\tilde{\mathbf{f}}}^{\mathrm{s}}_{\mathrm{b}}(k_y,\omega) \tag{4}$$

where a tilde above a variable denotes its representation in the frequency–wavenumber domain. This equilibrium equation is similar to the 3D coupled FE–BE equation (1), except that the stiffness matrices, the displacement vector, and the load vectors become wavenumber dependent. Solving equation (4) provides the structural response $\underline{\tilde{\mathbf{u}}}_{\mathrm{b}}(k_y,\omega)$, corresponding to the soil displacements $\underline{\tilde{\mathbf{u}}}_{\mathrm{s}}(k_y,\omega)$ on the soil–structure interface Σ. The BE equations allow to retrieve the soil tractions $\underline{\tilde{\mathbf{t}}}_{\mathrm{s}}(k_y,\omega)$:

$$\underline{\tilde{\mathbf{t}}}_{\mathrm{s}}(k_y,\omega) = \widetilde{\mathbf{U}}^{-1}(k_y,\omega)\left(\widetilde{\mathbf{T}}(k_y,\omega) + \mathbf{I}\right) \underline{\tilde{\mathbf{u}}}_{\mathrm{s}}(k_y,\omega) \tag{5}$$

where $\widetilde{\mathbf{U}}(k_y,\omega)$ and $\widetilde{\mathbf{T}}(k_y,\omega)$ are wavenumber dependent BE matrices. The representation theorem expressed in the frequency–wavenumber domain finally allows for the computation of the radiated wavefield $\underline{\tilde{\mathbf{u}}}_{\mathrm{r}}(k_y,\omega)$ in the soil [1]. The latter corresponds to the discretized boundary integral equation (3), where each variable should be replaced by its wavenumber dependent counterpart:

$$\underline{\tilde{\mathbf{u}}}_{\mathrm{r}}(k_y,\omega) = \widetilde{\mathbf{U}}_{\mathrm{s}}(k_y,\omega)\underline{\tilde{\mathbf{t}}}_{\mathrm{s}}(k_y,\omega) - \widetilde{\mathbf{T}}_{\mathrm{s}}(k_y,\omega)\underline{\tilde{\mathbf{u}}}_{\mathrm{s}}(k_y,\omega) \tag{6}$$

The application of a 2.5D approach in the frequency–wavenumber domain implies that the equations have to be assembled and solved for each wavenumber k_y. The response in the frequency–spatial domain can finally be found by means of an inverse Fourier transform $\mathscr{F}^{-1}\left[\tilde{f}(k_y), y\right] = \frac{1}{2\pi}\int_{-\infty}^{+\infty} \tilde{f}(k_y) \exp\left(-ik_y y\right) \mathrm{d}k_y$ from the wavenumber k_y to the longitudinal coordinate y, using an efficient Filon quadrature scheme [26].

3. 2.5D coupled FE–BE method with spatial windowing

The spatial windowing technique has been presented by Villot et al. [14] to account for the finite size of a plane structure in sound transmission and radiation calculations. This section describes how this technique

can be incorporated in the 2.5D coupled FE–BE method to account for the finite length of a structure in dynamic SSI problems.

Consider a plane wave with a constant longitudinal wavenumber k_{y0} travelling along an infinite structure. The displacement field in the spatial domain yields:

$$\hat{u}(y,\omega) = \frac{1}{2\pi}\hat{u}_0(\omega)\exp\left(-ik_{y0}y\right) \tag{7}$$

while the wavenumber spectrum corresponds to a Dirac delta function at $k_y = k_{y0}$ (figure 2a):

$$\tilde{u}(k_y,\omega) = \int_{-\infty}^{+\infty} \frac{1}{2\pi}\hat{u}_0(\omega)\exp\left(-ik_{y0}y\right)\exp\left(ik_y y\right)\,\mathrm{d}y \tag{8}$$

$$= \hat{u}_0(\omega)\delta\left(k_y - k_{y0}\right) \tag{9}$$

A structure with a finite length L_y, situated between y_1 and $y_2 = y_1 + L_y$, is only able to contribute to the radiation of waves into the soil domain Ω_s from y_1 to y_2. The wavenumber spectrum of the displacement field is consequently determined by applying a forward Fourier transform to equation (7), restricting the integration in equation (8) to $y \in [y_1, y_2]$:

$$\tilde{u}_\mathrm{sw}(k_y,\omega) = \int_{y_1}^{y_2} \frac{1}{2\pi}\hat{u}_0(\omega)\exp\left(-ik_{y0}y\right)\exp\left(ik_y y\right)\,\mathrm{d}y \tag{10}$$

$$= \frac{1}{2\pi}\hat{u}_0(\omega)\frac{\exp\left[i\left(k_y - k_{y0}\right)y_2\right]}{i\left(k_y - k_{y0}\right)}\left(1 - \exp\left[-i\left(k_y - k_{y0}\right)L_y\right]\right) \tag{11}$$

with $\lim_{k_y \to k_{y0}} \tilde{u}_\mathrm{sw}(k_y,\omega) = \frac{1}{2\pi}\hat{u}_0(\omega)L_y$. The subscript 'sw' refers to a spatially windowed quantity. Equation (11) reveals that spatial windowing results in a distribution of the energy over the entire wavenumber range [14], while it was originally concentrated at $k_y = k_{y0}$. This is illustrated in figure 2.

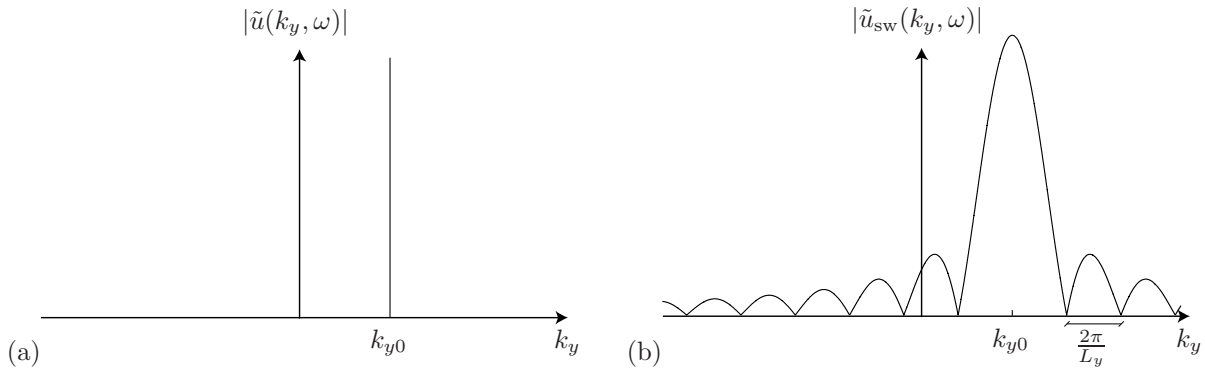

Figure 2: Wavenumber spectrum of a plane wave with wavenumber k_{y0} propagating in an infinite structure (a) before and (b) after application of the spatial windowing technique.

Application of the spatial windowing technique in the framework of the 2.5D FE–BE methodology outlined in subsection 2.2 implies that the contribution of each wavenumber component of the displacement vector $\underline{\tilde{\mathbf{u}}}_\mathrm{s}(k_y,\omega)$ is distributed over the entire wavenumber domain according to equation (11). The spatially windowed displacement vector $\underline{\tilde{\mathbf{u}}}_\mathrm{s,sw}(k_y,\omega)$ can hence be expressed as:

$$\underline{\tilde{\mathbf{u}}}_\mathrm{s,sw}(k_y,\omega) = \underline{\tilde{\mathbf{u}}}_\mathrm{s}(k_y,\omega) * \left[\frac{1}{2\pi}\frac{\exp\left(ik_y y_2\right)}{ik_y}\left(1 - \exp\left[-ik_y L_y\right]\right)\right] = \underline{\tilde{\mathbf{u}}}_\mathrm{s}(k_y,\omega) * \tilde{w}\left(k_y\right) \tag{12}$$

where $*$ indicates convolution. Spatially windowed interface tractions $\underline{\tilde{\mathbf{t}}}_\mathrm{s,sw}(k_y,\omega)$ are defined analogously. The radiated wavefield in the soil $\underline{\tilde{\mathbf{u}}}_\mathrm{r,sw}(k_y,\omega)$ is finally computed by means of the representation formula (6),

substituting $\tilde{\underline{\mathbf{u}}}_{\mathrm{s}}(k_y,\omega)$ and $\tilde{\underline{\mathbf{t}}}_{\mathrm{s}}(k_y,\omega)$ by their spatially windowed equivalents $\tilde{\underline{\mathbf{u}}}_{\mathrm{s,sw}}(k_y,\omega)$ and $\tilde{\underline{\mathbf{t}}}_{\mathrm{s,sw}}(k_y,\omega)$, respectively.

The windowing function $\tilde{w}(k_y)$ in equation (12) has zeros at $k_y = 2\pi n/L_y$, with $n = \pm1, \pm2, \pm3, \ldots$ A sufficiently fine wavenumber sampling is required for an accurate representation of the lobes of $\tilde{w}(k_y)$; the interval between two subsequent zeros $\Delta k_y = 2\pi/L_y$ (figure 2) is therefore discretized using 16 samples for all calculations presented in this paper. The resulting sampling of $\tilde{w}(k_y)$ hence depends on the length L_y and can be finer or coarser than the sampling of $\tilde{\underline{\mathbf{u}}}_{\mathrm{s}}(k_y,\omega)$ and $\tilde{\underline{\mathbf{t}}}_{\mathrm{s}}(k_y,\omega)$; either $\tilde{w}(k_y)$ or $\tilde{\underline{\mathbf{u}}}_{\mathrm{s}}(k_y,\omega)$ and $\tilde{\underline{\mathbf{t}}}_{\mathrm{s}}(k_y,\omega)$ needs to be upsampled before the convolution of equation (12) can be performed. A fine sampling of $\tilde{w}(k_y)$ is in particular required for very elongated structures, but the additional computational cost for upsampling $\tilde{\underline{\mathbf{u}}}_{\mathrm{s}}(k_y,\omega)$ and $\tilde{\underline{\mathbf{t}}}_{\mathrm{s}}(k_y,\omega)$ is negligible.

Equation (12) indicates that the spatial windowing technique only entails postprocessing of the original 2.5D results. A major limitation of the technique is, however, its inability to account for reflected waves generated at the boundaries of a finite structure to reproduce the resonant behaviour of the modes; only the diffraction due to a structure's finite length is considered.

4. Application of spatial windowing to elongated structures: vibration isolation screen

Numerical examples are considered in sections 4 and 5 to validate the spatial windowing technique and to investigate its applicability. The examples in section 4 involve structures of which one dimension is relatively large compared to the other dimensions, while this is not the case in section 5. For each case, a rigorous validation is provided by means of 3D calculations through the FE–$\mathscr{H}$-BE methodology mentioned in subsection 2.1. All calculations have been performed on Intel® Xeon® E5520 (2.26 GHz) CPUs.

The applications in subsections 4.1 and 4.2 are related to railway induced ground vibration, which can lead to vibration annoyance in buildings in close proximity of railway tracks. In order to reduce the levels of building vibration, mitigation measures on the transmission path between source (railway track) and receiver (building) can be implemented. Examples of such measures are vibration isolation screens [27], buried wall barriers [7], and wave impeding blocks [6]. In subsection 4.1, an open trench is discussed, which aims at reflecting the impinging waves and is known to be very effective for a trench depth greater than about 0.60 times the Rayleigh wavelength in the soil [27]. Trenches are assumed to be infinitely long in most of the numerical studies reported in the literature [28, 29, 30]; this assumption is not fulfilled in practice, however. A numerical and experimental study on trenches of finite length has been presented by Banerjee et al. [31]. It is shown next how the spatial windowing technique allows accounting for the finite length of the trench. As this merely involves postprocessing of the original 2.5D results, parametric studies to investigate the effect of a finite length can be performed at relatively low computational cost. The case of an in–filled trench will be discussed in subsection 4.2.

4.1. Open trench

The vibration reduction efficiency of an open trench in a halfspace is investigated in this subsection. The halfspace is characterized by a shear wave velocity $C_{\mathrm{s}} = 200\,\mathrm{m/s}$, a dilatational wave velocity $C_{\mathrm{p}} = 400\,\mathrm{m/s}$, a density $\rho = 2000\,\mathrm{kg/m^3}$, and material damping ratios $\beta_{\mathrm{s}} = \beta_{\mathrm{p}} = 0.025$ in deviatoric and volumetric deformation. The trench has a width $w = 2\,\mathrm{m}$, a depth $d = 2\,\mathrm{m}$, a length L_y, is situated at a distance $\mathscr{D} = 4\,\mathrm{m}$ from the y–axis, and is positioned symmetrically with respect to the x-axis, i.e. $y_1 = -L_y/2$ and $y_2 = L_y/2$ (figure 3a). The width of the trench is chosen in view of the case study of an in–filled trench that will be considered in subsection 4.2. The numerical analysis is performed for trenches with a length of 15 m, 30 m, and 60 m. The dimensionless trench depth $\bar{d}$ is defined as $d/\lambda_{\mathrm{R}}(f)$, where $\lambda_{\mathrm{R}}(f)$ is the frequency dependent Rayleigh wavelength in the soil; a value $\bar{d} = 0.60$ is obtained at 56 Hz. In order to facilitate physical interpretation, an incident wavefield is generated by the application of a unit vertical harmonic point load at the origin of the coordinate system, rather than considering a train passage.

The spatial windowing technique outlined in section 3 is used to calculate the wavefield in the soil, accounting for the presence of the open trench with length L_y. The interface Σ of the trench is modelled with 30 2.5D boundary elements; the element dimensions are limited in order to ensure that 10 elements

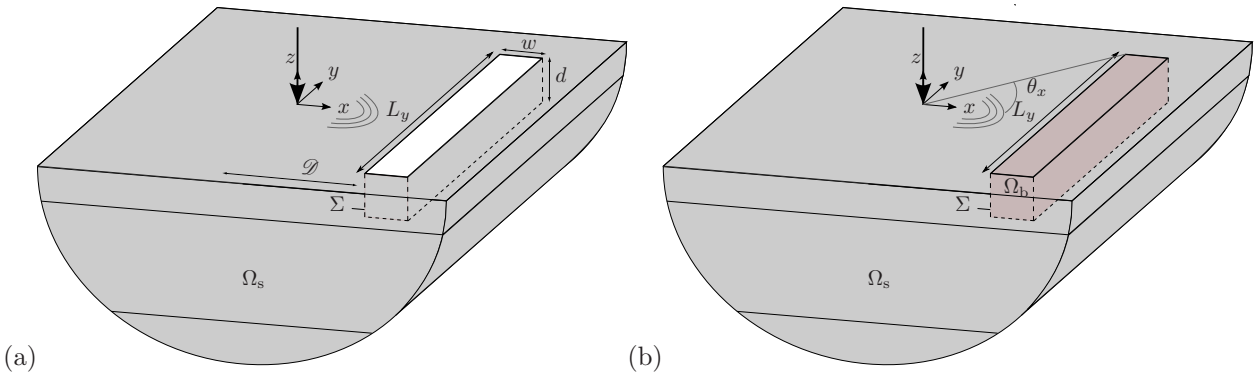

Figure 3: The soil domain Ω_s with (a) an open trench or (b) a block of stiffened soil Ω_b with finite length L_y.

per shear wavelength $\lambda_s = C_s/f$ are used at a frequency of 100 Hz. Coupling of the boundary elements to finite elements is not required, as no in–fill material is considered. The 2.5D computations with spatial windowing are compared to 3D $\mathscr{H}$-BE calculations, where four–node quadrilateral boundary elements are employed to discretize the interface Σ. The properties of the resulting 3D discretizations are listed in table 1; the last three columns are irrelevant for the present application. Eight elements per shear wavelength are provided at 100 Hz. Figures 4a and 4b show the BE discretization of an open trench with a length of 60 m used in the 2.5D BE model with spatial windowing and the 3D $\mathscr{H}$-BE model, respectively. These figures clearly illustrate that the 2.5D approach results in a significant reduction of the number of elements. The discretization of the free surface is avoided in both approaches by employing Green's functions for a halfspace in the 2.5D BE and 3D $\mathscr{H}$-BE formulations [1, 21].

L_y [m]	# BE elements [–]	# BE nodes [–]	# BE DOFs [–]	# FE elements [–]	# FE nodes [–]	# FE DOFs [–]
15	1568	1637	4911	3840	4941	14823
30	3008	3137	9411	7680	9801	29403
60	5888	6137	18411	15360	19521	58563

Table 1: Properties of the BE and FE discretizations of an open trench (only BE) or a block of stiffened soil (BE and FE) with a length of 15 m, 30 m, and 60 m.

The vibration reduction efficiency of a trench is characterized through the vertical insertion loss $\widehat{\mathrm{IL}}_z(\mathbf{x},\omega)$:

$$\widehat{\mathrm{IL}}_z(\mathbf{x},\omega) = 20\log_{10}\frac{|\hat{u}_z^{\mathrm{ref}}(\mathbf{x},\omega)|}{|\hat{u}_z(\mathbf{x},\omega)|} \tag{13}$$

which compares the vertical displacement $\hat{u}_z^{\mathrm{ref}}(\mathbf{x},\omega)$ in the reference case (without a trench) to the vertical displacement $\hat{u}_z(\mathbf{x},\omega)$ in case a trench is included; positive values of the insertion loss indicate a reduction of the vertical free field vibrations. Figures 5–7 show the insertion loss $\widehat{\mathrm{IL}}_z(\mathbf{x},\omega)$ for a trench with a length of 15 m, 30 m, and 60 m at 15 Hz, 30 Hz, and 60 Hz, respectively. The dimensionless trench depth equals $\bar{d} = 0.16$ at 15 Hz, $\bar{d} = 0.32$ at 30 Hz, and $\bar{d} = 0.64$ at 60 Hz. The insertion loss remains rather limited at 15 Hz, as a significant part of the energy still passes underneath the trench. The penetration depth of the Rayleigh waves decreases at higher frequencies, causing reflection of the waves by the trench and resulting in insertion losses up to 10 dB and more at 30 Hz and 60 Hz. Extending the length of the trench leads to an enlargement of the area where vibration levels are effectively reduced. The results are furthermore compared to rigorous 3D $\mathscr{H}$-BE calculations, and an almost perfect agreement between the spatially windowed 2.5D and the 3D computations is observed for all trench lengths and at all frequencies under concern. The

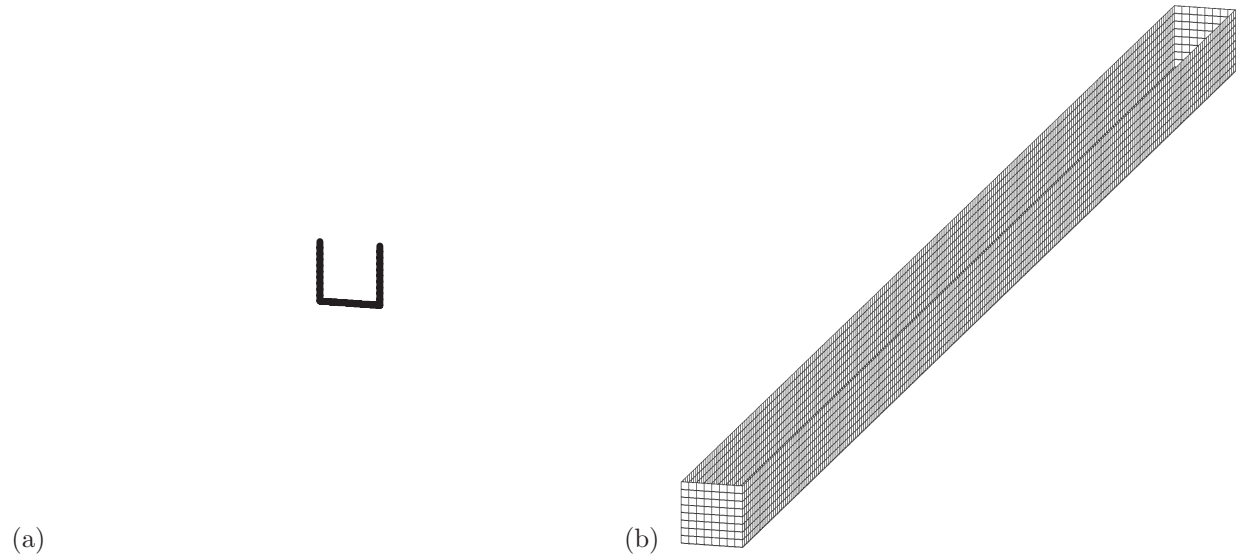

Figure 4: BE discretization of an open trench with a length of 60 m used in (a) the 2.5D BE model with spatial windowing and (b) the 3D $\mathscr{H}$-BE model.

correspondence is not only apparent at the surface of the halfspace, but also at depth. A quantitative assessment of the accuracy of the spatial windowing technique is given in figure 8. This figure shows the relative error $\hat{\varepsilon}(\mathbf{x},\omega)$, which is defined as:

$$\hat{\varepsilon}(\mathbf{x},\omega) = \frac{|\hat{u}_{z,\mathrm{sw}}(\mathbf{x},\omega) - \hat{u}_z(\mathbf{x},\omega)|}{|\hat{u}_{z\mathrm{i}}(\mathbf{x},\omega)|} \tag{14}$$

where $\hat{u}_{z,\mathrm{sw}}(\mathbf{x},\omega)$ and $\hat{u}_z(\mathbf{x},\omega)$ represent the vertical displacement obtained with a 2.5D model with spatial windowing and a 3D model, respectively, while $\hat{u}_{z\mathrm{i}}(\mathbf{x},\omega)$ is the incident wavefield. The error $|\hat{u}_{z,\mathrm{sw}}(\mathbf{x},\omega) - \hat{u}_z(\mathbf{x},\omega)|$ is normalized in equation (14) with respect to the incident wavefield $\hat{u}_{z\mathrm{i}}(\mathbf{x},\omega)$ instead of $\hat{u}_z(\mathbf{x},\omega)$; this avoids a blow up of $\hat{\varepsilon}(\mathbf{x},\omega)$ if $\hat{u}_z(\mathbf{x},\omega)$ attains a very small value, which is especially the case behind the trench. It is clear in figure 8 that the error is negligibly small at 15 Hz for all trench lengths. The error also remains limited at higher frequencies, although some larger deviations (up to 50%) can be observed in concentrated areas, mainly near the trench's edges. The error is sufficiently small in the main region of interest (i.e. just behind the trench) to conclude that the proposed spatial windowing technique is capable of accurately accounting for the finite length of the trench. As there is no in–fill material in the open trench, the wavefield in the soil cannot be affected by the resonant behaviour of structural modes, explaining why the spatial windowing technique is particularly well suited for the case under concern. The existence of structural modes might affect the accuracy of the proposed technique, however, as will be investigated in the following subsection.

The 2.5D calculations based on the assumption of longitudinal invariance (i.e. without spatial windowing) are shown in figures 5–7d. A comparison of figures 5–7a–c and 5–7d clearly indicates that accounting for the finite length of the trench is important to correctly assess the vibration reduction efficiency. A trench of limited length is only able to reflect that part of the wavefield that impinges on the trench, which is clearly visible for a trench of 15 m (figures 5–7a). Furthermore, diffraction around the edges of a finite trench leads to a decreased efficiency in part of the shadow zone. Both phenomena are accounted for in the spatial windowing technique.

The results can also be interpreted by considering the insertion loss $\widetilde{\mathrm{IL}}_z(x,\bar{k}_y,z,\omega)$ in the frequency–wavenumber domain. The latter is defined in a similar way as in equation (13), but now for the frequency–wavenumber domain representation of the vertical free field displacement. The dimensionless wavenumber

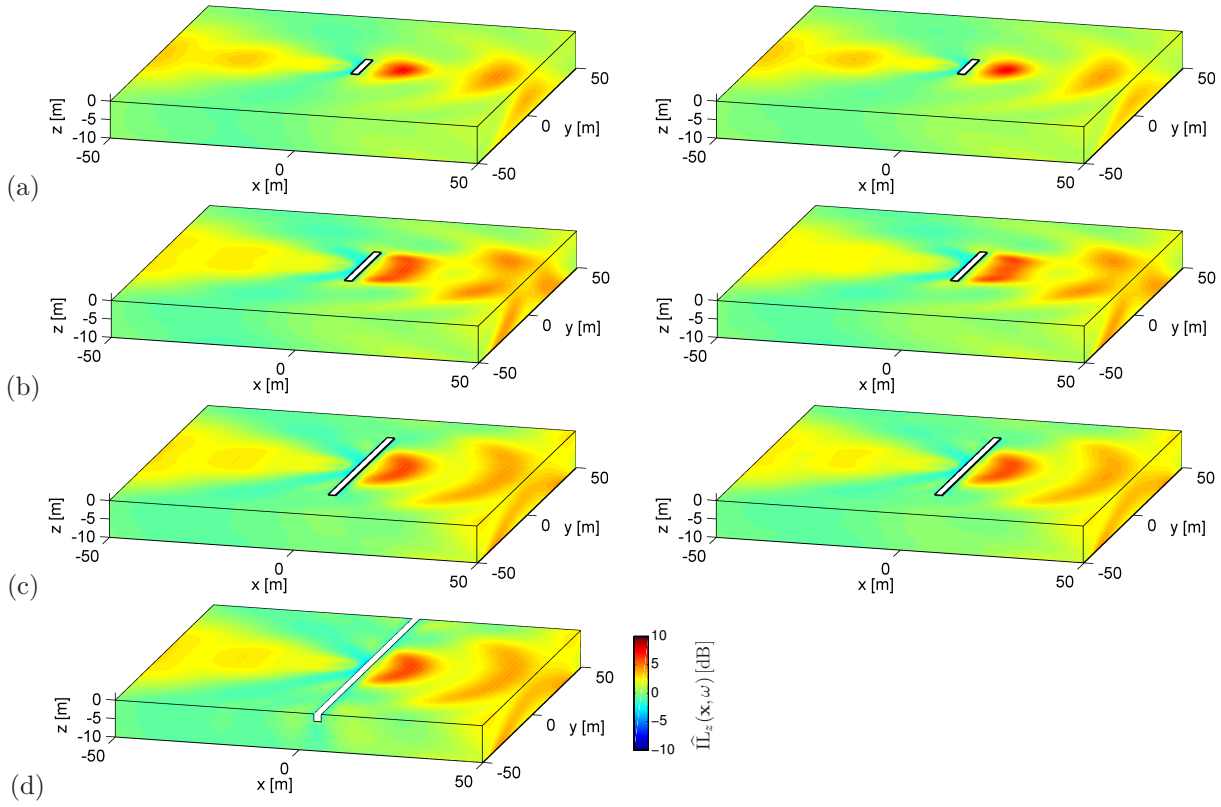

Figure 5: Vertical insertion loss $\widehat{\mathrm{IL}}_z(\mathbf{x},\omega)$ at 15 Hz for an open trench in a halfspace with a length (a) $L_y = 15\,\mathrm{m}$, (b) $L_y = 30\,\mathrm{m}$, (c) $L_y = 60\,\mathrm{m}$, and (d) $L_y = \infty$, calculated by means of a 2.5D BE model with spatial windowing (left hand side) or a 3D $\mathscr{H}$-BE model (right hand side).

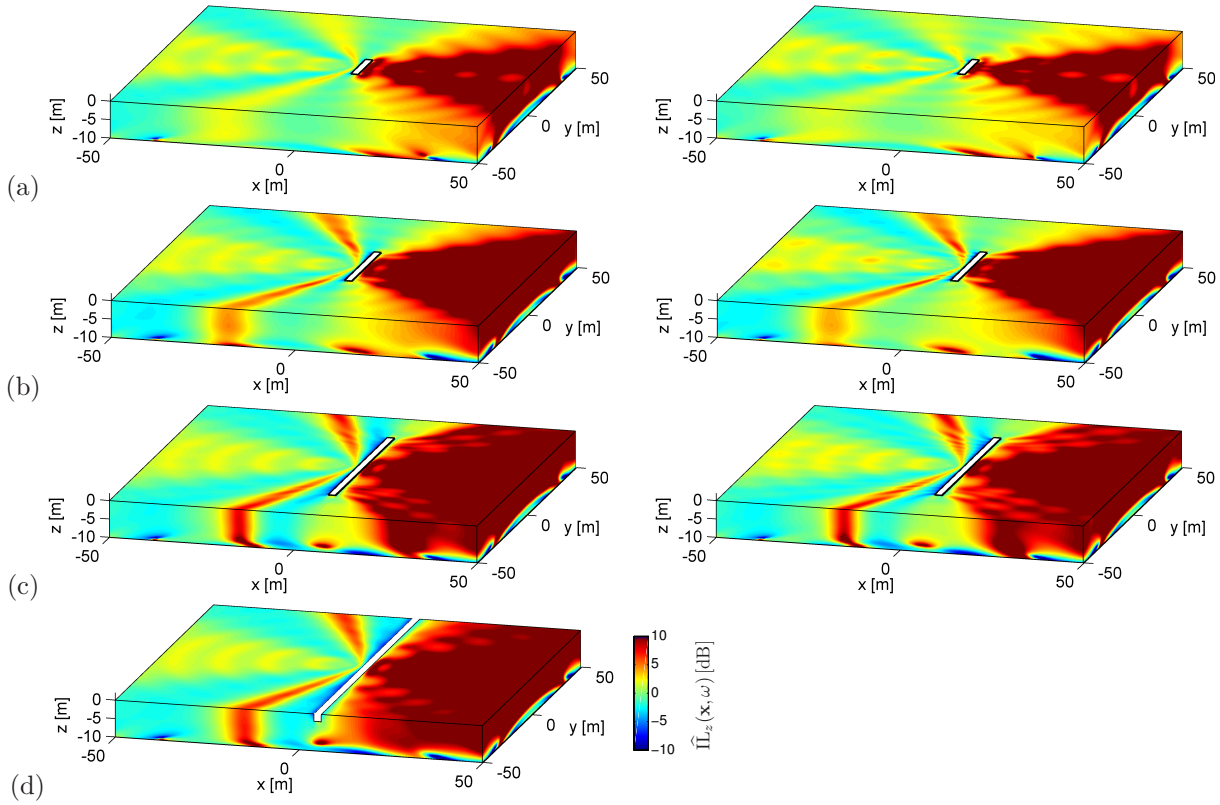

Figure 6: Vertical insertion loss $\widehat{\mathrm{IL}}_z(\mathbf{x},\omega)$ at 30 Hz for an open trench in a halfspace with a length (a) $L_y = 15\,\mathrm{m}$, (b) $L_y = 30\,\mathrm{m}$, (c) $L_y = 60\,\mathrm{m}$, and (d) $L_y = \infty$, calculated by means of a 2.5D BE model with spatial windowing (left hand side) or a 3D $\mathscr{H}$-BE model (right hand side).

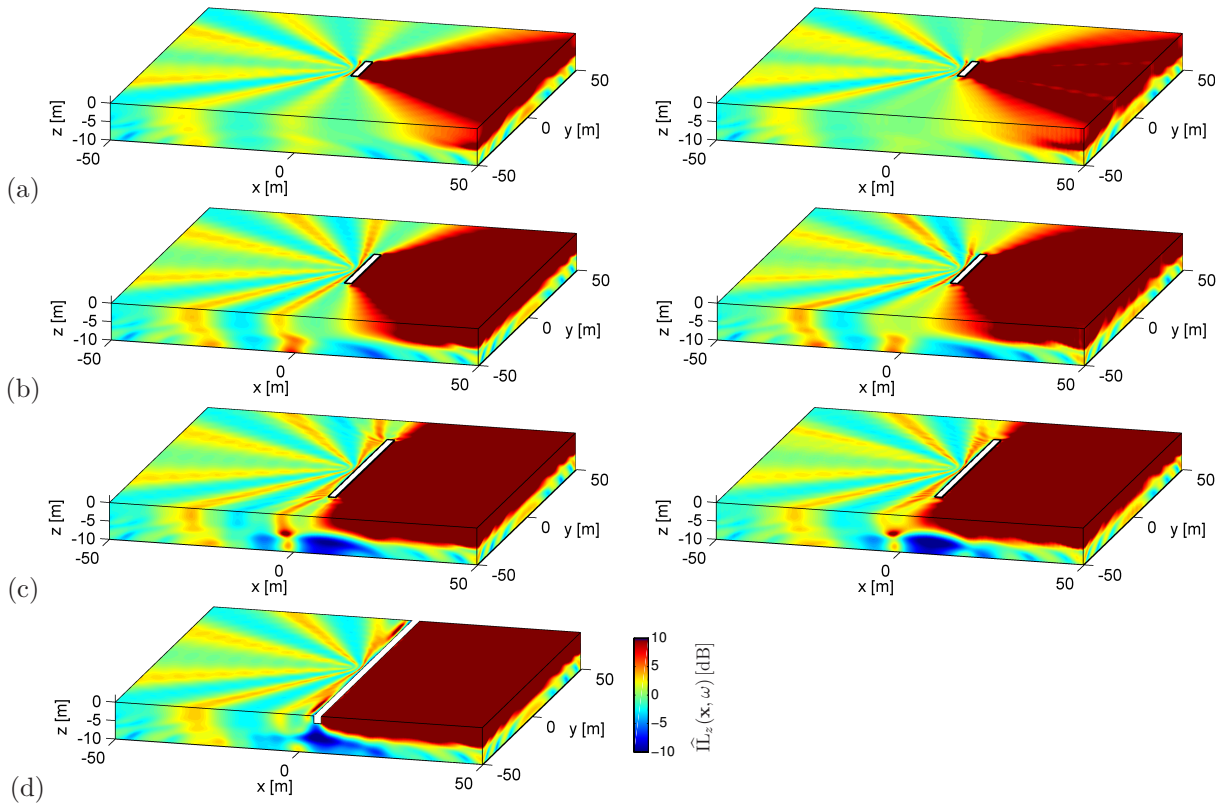

Figure 7: Vertical insertion loss $\widehat{\mathrm{IL}}_z(\mathbf{x},\omega)$ at 60 Hz for an open trench in a halfspace with a length (a) $L_y = 15\,\mathrm{m}$, (b) $L_y = 30\,\mathrm{m}$, (c) $L_y = 60\,\mathrm{m}$, and (d) $L_y = \infty$, calculated by means of a 2.5D BE model with spatial windowing (left hand side) or a 3D $\mathscr{H}$-BE model (right hand side).

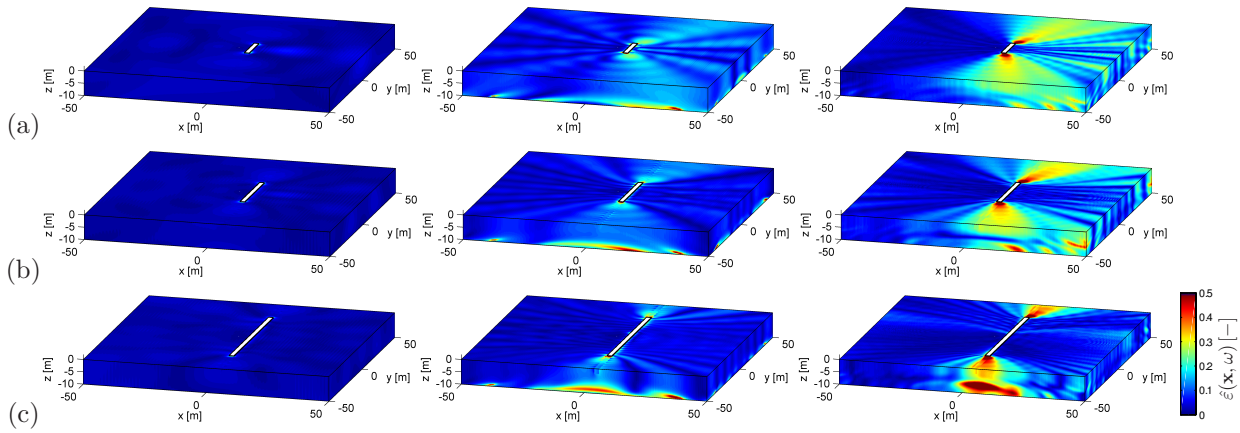

Figure 8: Relative error $\hat{\varepsilon}(\mathbf{x},\omega)$ for an open trench in a halfspace with a length (a) $L_y = 15\,\mathrm{m}$, (b) $L_y = 30\,\mathrm{m}$, and (c) $L_y = 60\,\mathrm{m}$ at 15 Hz (left), 30 Hz (middle), and 60 Hz (right).

$\bar{k}_y$ is defined as $\bar{k}_y = k_y C_\mathrm{s}/\omega$, where C_s is the shear wave velocity of the halfspace. Figure 9d shows the insertion loss $\widetilde{\mathrm{IL}}_z(x = 8\,\mathrm{m}, \bar{k}_y, z = 0\,\mathrm{m}, \omega)$ on the surface of the halfspace at 8 m from the point of excitation for an infinitely long open trench in a halfspace; the insertion loss is only shown in a range $0 \leq \bar{k}_y \leq \bar{k}_\mathrm{R}$, with $\bar{k}_\mathrm{R} = C_\mathrm{s}/C_\mathrm{R}$ the dimensionless wavenumber corresponding to a Rayleigh wave propagating in the y-direction. Outside this range, waves do not propagate in the x-direction, as the lateral wavenumber $\bar{k}_x = -i\sqrt{\bar{k}_y^2 - \bar{k}_\mathrm{R}^2}$ is imaginary for $\bar{k}_y > \bar{k}_\mathrm{R}$, resulting in evanescent waves. The dispersion curve of a Rayleigh wave propagating in the y-direction is a horizontal line due to its non–dispersive character in a homogeneous halfspace. It is observed in figure 9d that no significant reduction of vibration levels can be achieved below 20 Hz, as the dimensionless trench depth $\bar{d}$ is only 0.20 at this frequency. The insertion loss increases up to 4 to 6 dB in the frequency range between 20 Hz and 45 Hz, while it tends to 10 dB and more above 45 Hz. This frequency corresponds to a dimensionless trench depth $\bar{d} = 0.50$, approximately confirming the rule of thumb which states that an open trench is effective from $\bar{d} = 0.60$ on [27].

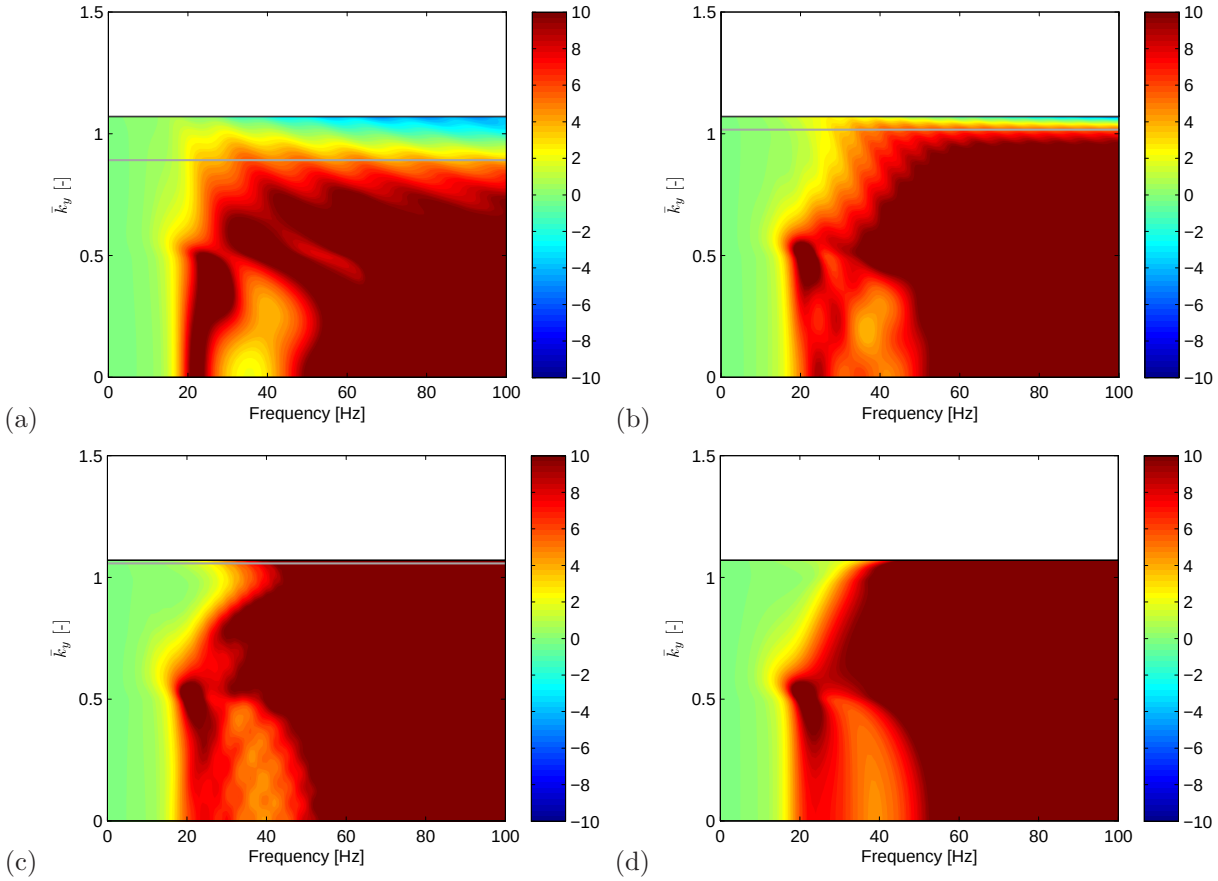

Figure 9: Vertical insertion loss $\widetilde{\mathrm{IL}}_z(x = 8\,\mathrm{m}, \bar{k}_y, z = 0\,\mathrm{m}, \omega)$ for an open trench in a halfspace with a length (a) $L_y = 15\,\mathrm{m}$, (b) $L_y = 30\,\mathrm{m}$, (c) $L_y = 60\,\mathrm{m}$, and (d) $L_y = \infty$, calculated by means of a 2.5D BE model with spatial windowing. Superimposed are the dispersion curve of a Rayleigh wave in the y-direction (black line) and the curve $\bar{k}_y = \bar{k}_\mathrm{R} \sin\theta_x$ (grey line).

Figures 9a–c show the insertion loss $\widetilde{\mathrm{IL}}_z(x = 8\,\mathrm{m}, \bar{k}_y, z = 0\,\mathrm{m}, \omega)$ for an open trench in a halfspace with a length of 15 m, 30 m, or 60 m, respectively; these results are obtained by means of the spatial windowing technique. The displacements on the interface Σ that are used for the determination of the vertical displacement $\tilde{u}_z(x = 8\,\mathrm{m}, \bar{k}_y, z = 0\,\mathrm{m}, \omega)$ in the soil and the corresponding insertion loss $\widetilde{\mathrm{IL}}_z(x = 8\,\mathrm{m}, \bar{k}_y, z = 0\,\mathrm{m}, \omega)$ in figure 9d are thus first modified by the convolution operation defined in equation (12) and are

subsequently used in the representation formula (6) for the computation of $\tilde{u}_{z,\mathrm{sw}}(x = 8\,\mathrm{m}, \bar{k}_y, z = 0\,\mathrm{m}, \omega)$ and the insertion loss $\widetilde{\mathrm{IL}}_z(x = 8\,\mathrm{m}, \bar{k}_y, z = 0\,\mathrm{m}, \omega)$ in figures 9a–c. As indicated above, a trench of finite length is only able to reflect that part of the wavefield that actually impinges on the trench and no reduction of vibration levels is achieved for wavenumbers $\bar{k}_y$ larger than $\bar{k}_\mathrm{R} \sin\theta_x$, where $\sin\theta_x$ corresponds to (figure 3):

$$\sin\theta_x = \frac{L_y/2}{\sqrt{\mathscr{D}^2 + (L_y/2)^2}} \tag{15}$$

This is confirmed in figures 9a–c, as the insertion loss in the $(\omega, \bar{k}_y)$–domain remains limited for $\bar{k}_y > \bar{k}_\mathrm{R} \sin\theta_x$.

The computational effort for the 2.5D computations (with or without spatial windowing) is considerably lower than for the full 3D calculations, as is demonstrated in tables 2 and 3. Table 2 summarizes the amount of RAM memory required for the storage of the BE matrices $\widetilde{\mathbf{U}}(k_y, \omega)$ and $\widetilde{\mathbf{T}}(k_y, \omega)$ or $\widehat{\mathbf{U}}(\omega)$ and $\widehat{\mathbf{T}}(\omega)$ in the 2.5D BE or 3D $\mathscr{H}$-BE models, respectively. The amount of RAM memory that would have been required in a classical 3D BE model without the application of $\mathscr{H}$–matrices is indicated as well. It is clearly illustrated in table 2 that the 2.5D approach results in a substantial reduction of the required RAM memory. The efficiency in terms of computation time is assessed in table 3. The computation time for a 3D open trench with a length of $L_y = 15\,\mathrm{m}$ is comparable to that of a 2.5D calculation, while it significantly exceeds the latter for larger trench lengths. As the 2.5D equations are solved independently for each wavenumber k_y in the frequency–wavenumber domain, the 2.5D calculations can easily be parallelized. The use of MATLAB's Parallel Computing Toolbox [32] allows for a distributed computation on eight cores, leading to a speed–up by a factor that is slightly less than eight (due to the communication overhead). The value of 1.8 h listed in table 3 indicates the total computation time on all cores; the actual computation time is only 0.25 h. A similar parallelization can not be applied to the 3D $\mathscr{H}$-BE models, however.

		15 Hz	30 Hz	60 Hz
2.5D	$\widetilde{\mathbf{U}}(k_y, \omega)$	0.55	0.55	0.55
	$\widetilde{\mathbf{T}}(k_y, \omega)$	0.55	0.55	0.55
3D ($L_y = 15\,\mathrm{m}$)	$\widehat{\mathbf{U}}(\omega)$	164 (368)	170 (368)	186 (368)
	$\widehat{\mathbf{T}}(\omega)$	174 (368)	176 (368)	194 (368)
3D ($L_y = 30\,\mathrm{m}$)	$\widehat{\mathbf{U}}(\omega)$	348 (1351)	363 (1351)	419 (1351)
	$\widehat{\mathbf{T}}(\omega)$	371 (1351)	380 (1351)	524 (1351)
3D ($L_y = 60\,\mathrm{m}$)	$\widehat{\mathbf{U}}(\omega)$	793 (5172)	925 (5172)	1437 (5172)
	$\widehat{\mathbf{T}}(\omega)$	847 (5172)	1380 (5172)	1743 (5172)

Table 2: RAM memory (in MB) required for the storage of the BE matrices $\widetilde{\mathbf{U}}(k_y, \omega)$ and $\widetilde{\mathbf{T}}(k_y, \omega)$ or $\widehat{\mathbf{U}}(\omega)$ and $\widehat{\mathbf{T}}(\omega)$ in the 2.5D BE or 3D $\mathscr{H}$-BE models of an open trench and a stiff wave barrier. The amount of RAM memory that would have been required in classical 3D BE models without the application of $\mathscr{H}$–matrices is given between brackets.

	15 Hz	30 Hz	60 Hz
2.5D	1.8	1.8	1.8
3D ($L_y = 15\,\mathrm{m}$)	2.0	2.0	2.1
3D ($L_y = 30\,\mathrm{m}$)	2.6	2.6	2.7
3D ($L_y = 60\,\mathrm{m}$)	4.3	4.6	5.5

Table 3: Computation time (in hours) required for the 2.5D BE or 3D $\mathscr{H}$-BE calculations involving an open trench in a halfspace.

4.2. Stiff wave impeding vibration barrier

For stability reasons, the construction of an open trench in the soil is limited to shallow depths; the use of either soft or stiff in–fill materials allows for an increase of depth. If a soft in–fill material is used, the behaviour of a filled trench resembles that of an open trench [30]. The use of a stiff in–fill material, however, fundamentally alters the physical mechanism that leads to a reduction of vibration levels. A recent investigation using a 2.5D approach has revealed that a vibration isolation screen with a stiff in–fill material (e.g. created by means of jet grouting) can act as a wave impeding barrier [33]; the effectiveness depends on the stiffness contrast between the soil and the in–fill material.

The spatial windowing technique proposed in this paper allows assessing the vibration reduction efficiency for a jet grouting wall of finite length (figure 3b). The case study of an open trench discussed in subsection 4.1 is reconsidered, introducing an in–fill material with a shear wave velocity $C_\mathrm{s} = 550\,\mathrm{m/s}$ and a dilatational wave velocity $C_\mathrm{p} = 950\,\mathrm{m/s}$; the same density and material damping ratios as in the halfspace are used. The 2.5D boundary elements are now coupled to a conforming mesh of 2.5D finite elements to model the block of stiffened soil. 3D FE–$\mathscr{H}$-BE validation calculations are performed as well, coupling eight–node solid finite elements to four–node quadrilateral boundary elements. The properties of the 3D discretizations are summarized in table 1. The 2.5D and 3D finite element discretizations result in 27.5 or 22 elements per shear wavelength in the barrier at 100 Hz, respectively.

Figures 10–12 show the insertion loss $\widehat{\mathrm{IL}}_z(\mathbf{x},\omega)$ that is achieved by the inclusion of a block of stiffened soil with a length of 15 m, 30 m, and 60 m in the halfspace at a frequency of 15 Hz, 30 Hz, and 60 Hz, respectively. The results of the 2.5D FE–BE models with spatial windowing are compared to the 3D FE–$\mathscr{H}$-BE computations and, as in subsection 4.1, a good correspondence between the models is observed. Some discrepancies are apparent, however, especially if a block with a length of 15 m is considered at 60 Hz (figure 12a). The relative error $\hat{\varepsilon}(\mathbf{x},\omega)$, defined in equation (14), is shown in figure 13 for a quantitative comparison in each of these cases. The error is negligibly small at 15 Hz for all barrier lengths and remains limited at higher frequencies for barrier lengths of 30 m and 60 m, except near the barrier's edges. A much larger discrepancy between the 2.5D results with spatial windowing and the 3D results is revealed for a barrier of 15 m at 60 Hz, however.

The observed discrepancies can be attributed to the modal behaviour of the finite block, which is not accounted for by the spatial windowing technique. This is investigated in figure 14. Figure 14a shows the mode count $N(f)$ for each of the stiff wave barriers considered above. An increasing length of the block results in a larger number of flexible modes within the frequency range between 0 and 100 Hz. The distribution of the natural frequencies in the frequency domain is characterized by the modal density $n(f) = \mathrm{d}N(f)/\mathrm{d}f$ [34]. In order to evaluate the latter, a continuous function is fitted through the discrete curve. In the low frequency range, the dynamic response is dominated by the resonating behaviour of individual modes. At higher frequencies, however, the response is determined by multiple overlapping modes and the contribution of individual modes can no longer be distinguished [34]. The transition from the low to the high frequency regime is quantified through the modal overlap $M(f) = \eta f n(f)$, where $\eta = 2\beta_\mathrm{s}$ is the loss factor; a modal overlap $M = 1$ is commonly chosen as the limit of the low frequency range [34]. Figure 14b shows the modal overlap $M(f)$ for a block of stiffened soil with a length of 15 m, 30 m, and 60 m. It is observed that the modal overlap increases with the block length; individual modes are only expected to dominate the response below 95 Hz, 45 Hz, and 20 Hz, respectively. This explains why the spatial windowing technique gives a better correspondence with the 3D FE–$\mathscr{H}$-BE computations if applied to a stiff wave barrier with a larger length. Even in the low frequency range ($M(f) < 1$), however, the overall influence of the resonating behaviour of individual modes remains rather limited due to the strong dynamic SSI (i.e. due to the associated radiation damping in the soil). This indicates that the proposed technique is an accurate and efficient tool to account for the finite length of the block of stiffened soil.

The 3D results are also compared to 2.5D results based on the assumption of longitudinal invariance (figures 10–12d). At 15 Hz, neither a length of 15 m or 30 m is sufficient to create a wave impeding effect similar to the case where the block is assumed to be of infinite length; implementing the block over a length of 60 m, however, does results in a comparable insertion loss. The insertion loss at 30 Hz resembles the result of the 2.5D calculation from a length of 30 m on, while a good correspondence with the latter is achieved for all lengths at a frequency of 60 Hz.

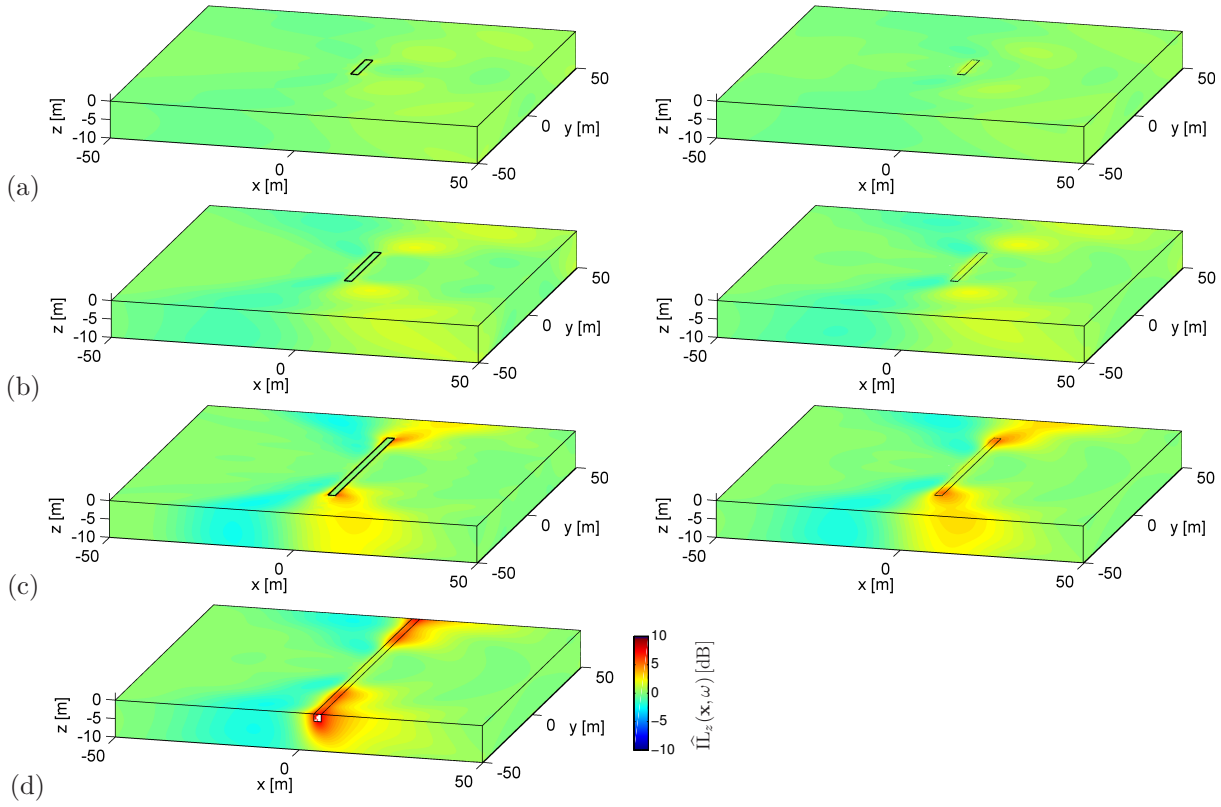

Figure 10: Vertical insertion loss $\widehat{\mathrm{IL}}_z(\mathbf{x},\omega)$ at 15 Hz for a block of stiffened soil in a halfspace with a length (a) $L_y = 15\,\mathrm{m}$, (b) $L_y = 30\,\mathrm{m}$, (c) $L_y = 60\,\mathrm{m}$, and (d) $L_y = \infty$, calculated by means of a 2.5D FE–BE model with spatial windowing (left hand side) or a 3D FE–$\mathscr{H}$-BE model (right hand side).

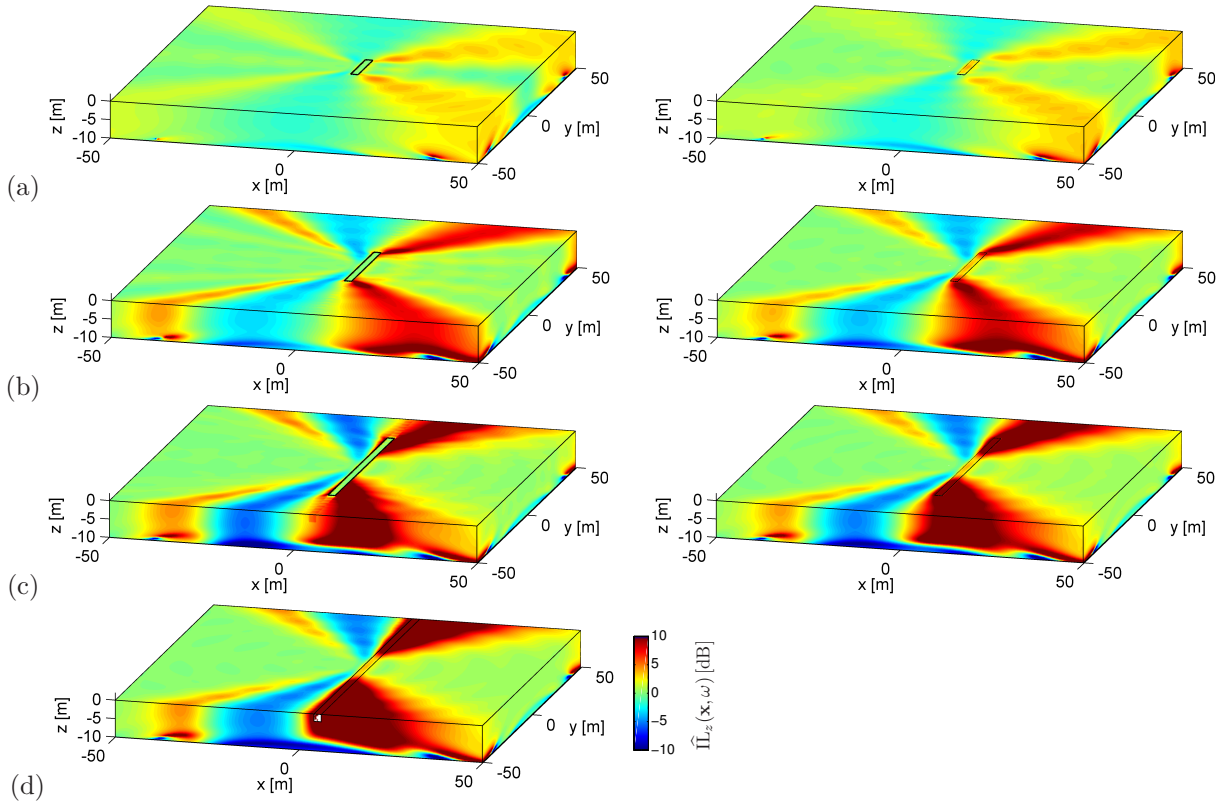

Figure 11: Vertical insertion loss $\widehat{\mathrm{IL}}_z(\mathbf{x},\omega)$ at 30 Hz for a block of stiffened soil in a halfspace with a length (a) $L_y = 15\,\mathrm{m}$, (b) $L_y = 30\,\mathrm{m}$, (c) $L_y = 60\,\mathrm{m}$, and (d) $L_y = \infty$, calculated by means of a 2.5D FE–BE model with spatial windowing (left hand side) or a 3D FE–$\mathscr{H}$-BE model (right hand side).

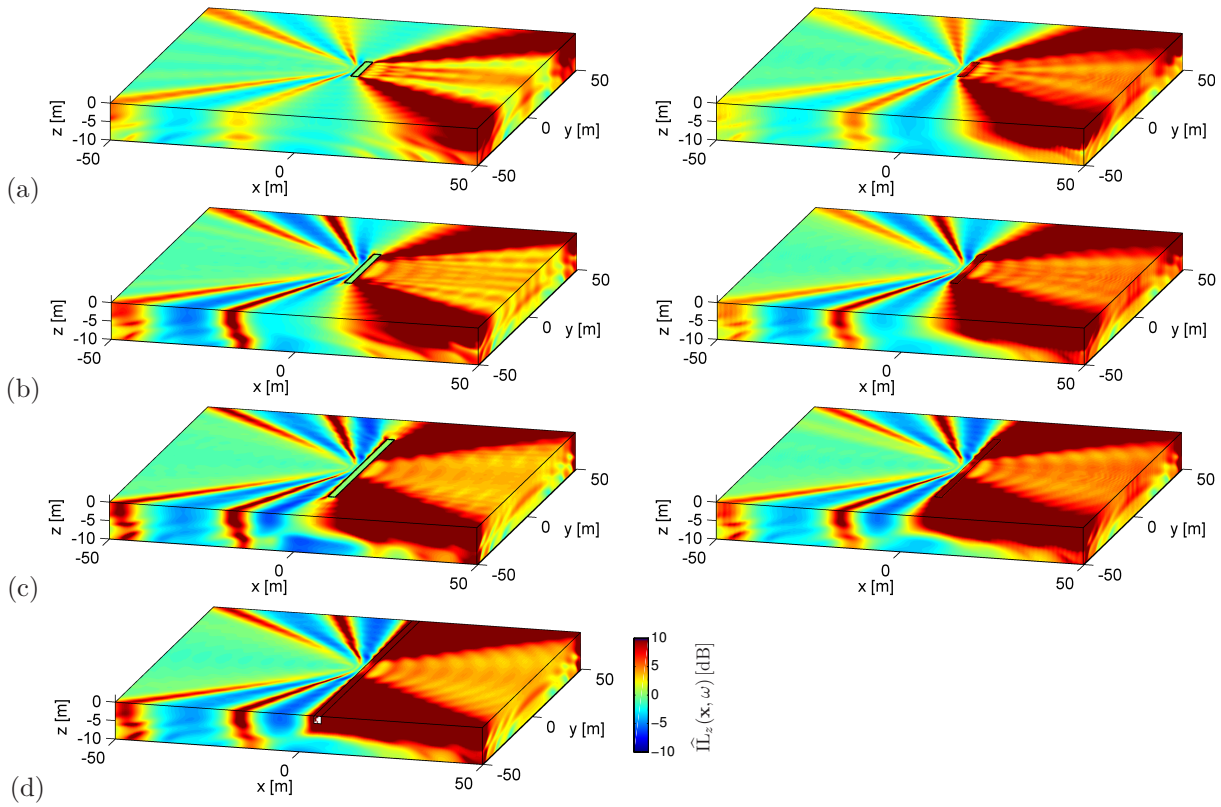

Figure 12: Vertical insertion loss $\widehat{\mathrm{IL}}_z(\mathbf{x},\omega)$ at 60 Hz for a block of stiffened soil in a halfspace with a length (a) $L_y = 15\,\mathrm{m}$, (b) $L_y = 30\,\mathrm{m}$, (c) $L_y = 60\,\mathrm{m}$, and (d) $L_y = \infty$, calculated by means of a 2.5D FE–BE model with spatial windowing (left hand side) or a 3D FE–$\mathscr{H}$-BE model (right hand side).

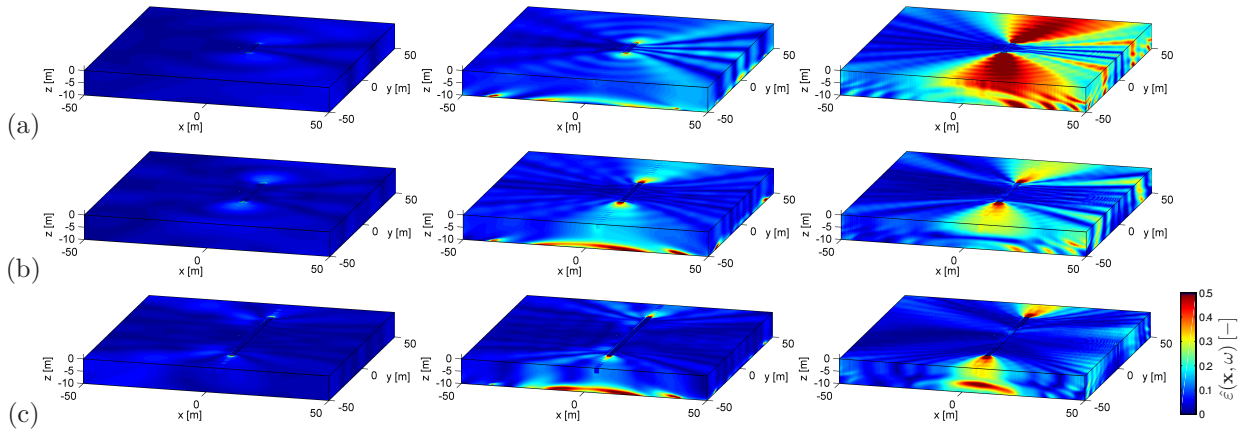

Figure 13: Relative error $\hat{\varepsilon}(\mathbf{x},\omega)$ for a block of stiffened soil in a halfspace with a length (a) $L_y = 15\,\mathrm{m}$, (b) $L_y = 30\,\mathrm{m}$, and (c) $L_y = 60\,\mathrm{m}$ at 15 Hz (left), 30 Hz (middle), and 60 Hz (right).

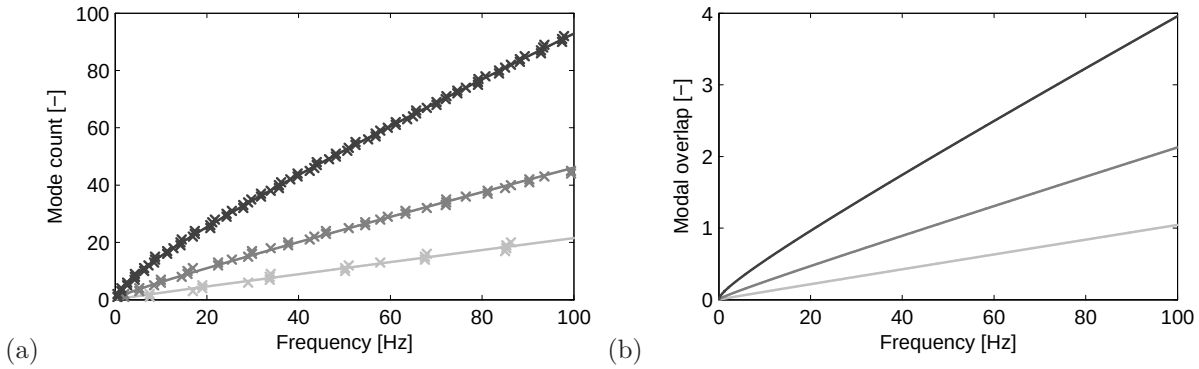

Figure 14: (a) Discrete (crosses) and fitted (solid line) mode count $N(f)$ and (b) modal overlap $M(f)$, for a block of stiffened soil with a length of 15 m, 30 m, and 60 m (light to dark grey lines).

The observations in figures 10–12 can be explained by considering the insertion loss $\widetilde{\mathrm{IL}}_z(x, \bar{k}_y, z, \omega)$ in the frequency–wavenumber domain. Figure 15d shows the insertion loss $\widetilde{\mathrm{IL}}_z(x = 8\,\mathrm{m}, \bar{k}_y, z = 0\,\mathrm{m}, \omega)$ for an infinitely long block of stiffened soil in a halfspace; the insertion loss is only shown in a range $0 \leq \bar{k}_y \leq \bar{k}_\mathrm{R}$. Superimposed on figure 15d is the dispersion curve $\bar{k}_y = \bar{k}_\mathrm{b}(\omega)$ of a free bending wave in an infinitely long Timoshenko beam with the same properties as the block of stiffened soil [35]. The region where a substantial insertion loss is obtained in the $(\omega, \bar{k}_y)$–domain is clearly bounded by the Rayleigh wave dispersion curve $\bar{k}_y = \bar{k}_\mathrm{R}$ and the free bending wave dispersion curve $\bar{k}_y = \bar{k}_\mathrm{b}(\omega)$. As reported in [33], the transmission of propagating plane waves with a wavenumber $\bar{k}_y$ larger than $\bar{k}_\mathrm{b}(\omega)$ (i.e. with a trace wavelength λ_y smaller than $\lambda_\mathrm{b}(\omega)$) is impeded by the block of stiffened soil, as the admittance of a beam of infinite length is then dominated by its bending stiffness and decreases proportionally to $\bar{k}_y^{-4}$ at a given radial frequency ω [35]. The intersection of the Rayleigh wave and the free bending wave dispersion curves hence determines the critical radial frequency from which the block of stiffened soil can act as a wave impeding barrier; a value of $2\pi \times 12\,\mathrm{Hz}$ is obtained in the present case [33]. In the spatial domain, a reduction of vibration levels is only achieved in an area delimited by a critical angle $\theta_\mathrm{c}(\omega) = \sin^{-1}\left(\bar{k}_\mathrm{b}(\omega)/\bar{k}_\mathrm{R}\right)$, which can clearly be distinguished on figures 10–12d. An analytical expression for $\theta_\mathrm{c}(\omega)$ as a function of the geometric and dynamic properties of the stiff wave barrier is given in [33].

Figures 15a–c show the insertion loss $\widetilde{\mathrm{IL}}_z(x = 8\,\mathrm{m}, \bar{k}_y, z = 0\,\mathrm{m}, \omega)$ for a block of stiffened soil in a halfspace with a length of 15 m, 30 m, or 60 m, respectively; these results are obtained by means of the spatial windowing technique. Large insertion losses are only observed in a part of the region indicated on figure 15d. The explanation for this observation is twofold. First, a finite block is only able to impede the transmission of that part of the wavefield that actually impinges on the block, and no reduction of vibration levels is obtained for $\bar{k}_y > \bar{k}_\mathrm{R} \sin\theta_x$, where $\sin\theta_x$ is defined in equation (15). This is similar to the behaviour of a finite trench discussed in subsection 4.1. Second, the results indicate that the block should be approximately twice as long as the free bending wavelength $\lambda_\mathrm{b}(\omega)$ in order to develop a similar behaviour as a beam of infinite length and thus to hinder the transmission of plane waves with a longitudinal wavelength smaller than $\lambda_\mathrm{b}(\omega)$. Lines corresponding to these two additional conditions are superimposed on figures 15a–c, clearly delimiting a reduced area of significant insertion loss in the $(\omega, \bar{k}_y)$–domain. Both phenomena result in an upward shift of the critical frequency with respect to the case of an infinite length, yielding critical frequencies of 35.2 Hz, 22.9 Hz, and 14.7 Hz for lengths of 15 m, 30 m, and 60 m, respectively. Stiffening of the soil over a length of 60 m hence suffices to mimic the dynamic behaviour of a block of infinite length.

The FE discretization of the block of stiffened soil leads to sparse and symmetric stiffness and mass matrices; the required RAM memory for the storage of these matrices is rather limited. The memory usage associated with the BE discretization consequently remains dominant; a comparison between the 2.5D and 3D BE models is given in table 2. A comparison of the 2.5D FE–BE and 3D FE-$\mathscr{H}$-BE in terms of computation time is shown in table 4; the efficiency of the 2.5D approach is clear. The large computation

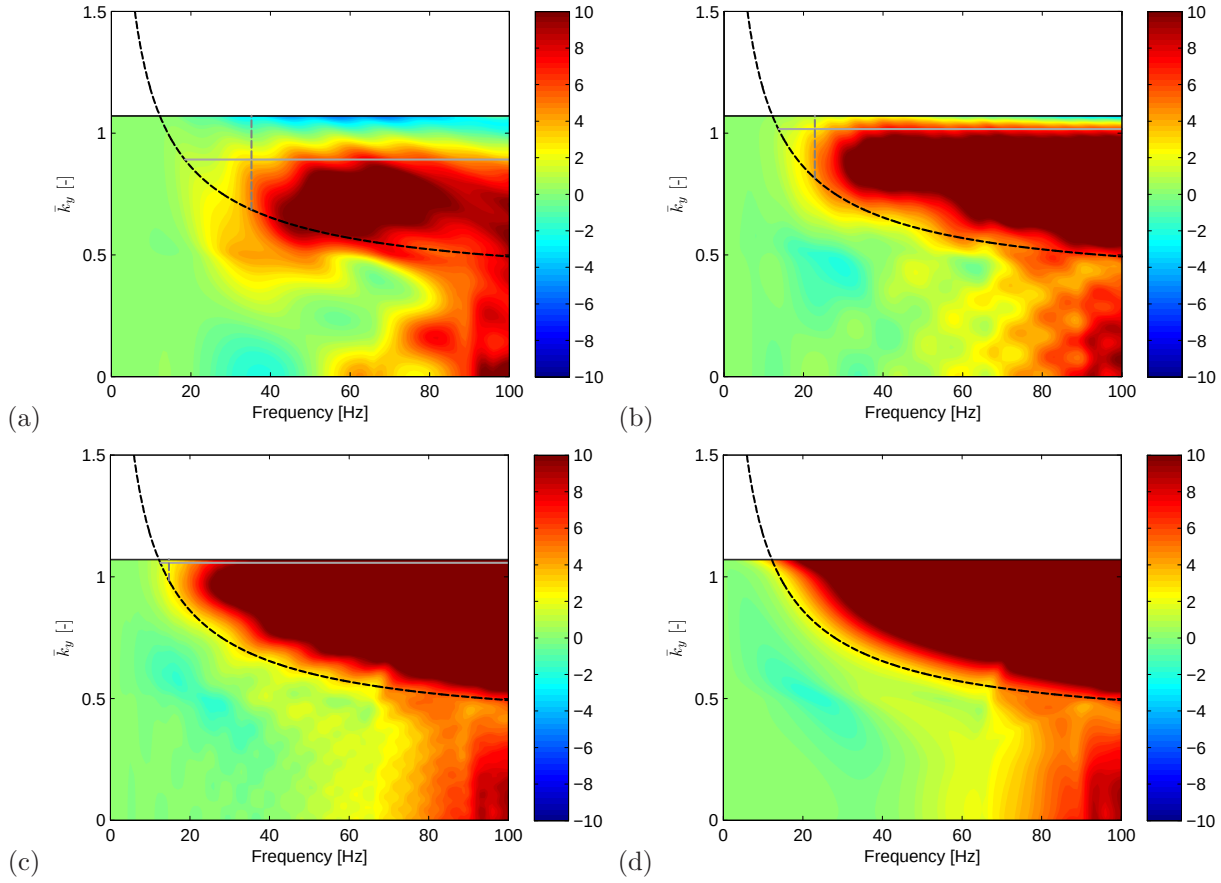

Figure 15: Vertical insertion loss $\widetilde{\mathrm{IL}}_z(x = 8\,\mathrm{m}, \bar{k}_y, z = 0\,\mathrm{m}, \omega)$ for a block of stiffened soil in a halfspace with a length (a) $L_y = 15\,\mathrm{m}$, (b) $L_y = 30\,\mathrm{m}$, (c) $L_y = 60\,\mathrm{m}$, and (d) $L_y = \infty$, calculated by means of a 2.5D FE–BE model with spatial windowing. Superimposed are the dispersion curve of a Rayleigh wave in the y-direction (solid black line), the free bending wave dispersion curve in an infinitely long beam (dashed black line), the curve $\bar{k}_y = \bar{k}_\mathrm{R} \sin\theta_x$ (solid grey line), and the curve $L_y = 2\lambda_\mathrm{b}(\omega)$ (dashed grey line).

times for a 3D stiff wave barrier with a length of 60 m are due to convergence difficulties in the iterative Neumann–Dirichlet FE–BE coupling algorithm. It should furthermore be noted that the computation time of the 2.5D models represents the total computation time on all eight cores used in the parallelized calculation; the actual computation time is only 0.30 h.

	15 Hz	30 Hz	60 Hz
2.5D	2.1	2.1	2.1
3D ($L_y = 15$ m)	2.5	2.3	2.3
3D ($L_y = 30$ m)	4.0	6.3	4.4
3D ($L_y = 60$ m)	24.4	12.6	13.2

Table 4: Computation time (in hours) required for the 2.5D FE–BE or 3D FE–$\mathscr{H}$-BE calculations involving a stiff wave barrier in a halfspace.

5. Application of spatial windowing to short structures: surface foundation

It has been demonstrated in subsections 4.1 and 4.2 that the proposed spatial windowing technique is an accurate and efficient tool to account for the finite length of structures. The validity of the methodology is now further explored in this section. The importance of the actual length of the structure, its modal behaviour, and the dynamic SSI are investigated. The structure under concern is a square surface foundation on a horizontally layered halfspace; the geometry thus strongly differs from the open trenches and stiff wave barriers previously discussed. In subsection 5.1, the flexibility is neglected and the foundation is modelled as a rigid body. The influence of flexible foundation modes on the accuracy of the methodology will subsequently be investigated in subsections 5.2 and 5.3.

5.1. Rigid surface foundation on a horizontally layered halfspace

The concrete foundation has a width $w = 5$ m, a length $L_y = 5$ m, a thickness $t = 0.25$ m, a Young's modulus $E = 33$ GPa, a Poisson's ratio $\nu = 0.20$, and a density $\rho = 2500\,\mathrm{kg/m^3}$. A hysteretic damping ratio $\beta = 0.03$ is included through application of the correspondence principle. The foundation is loaded by a unit harmonic vertical point load at its center. While a homogeneous halfspace has been considered in subsections 4.1 and 4.2 to facilitate physical interpretation, the soil in reality is often stratified; a layered halfspace is therefore included in this subsection. The soil consists of two layers on a halfspace, each with a thickness of 2 m. The shear wave velocity C_s is equal to 150 m/s in the top layer, 250 m/s in the second layer, and 300 m/s in the underlying halfspace. The Poisson's ratio ν is 1/3 everywhere, resulting in dilatational wave velocities C_p of 300 m/s, 500 m/s, and 600 m/s, respectively. Material damping ratios $\beta_\mathrm{s} = \beta_\mathrm{p} = 0.025$ in deviatoric and volumetric deformation are attributed to the layers and the halfspace, while a uniform density $\rho = 1800\,\mathrm{kg/m^3}$ is considered throughout the medium.

The spatial windowing technique is employed to compute the response of the foundation and the wavefield in the soil based on a 2.5D calculation. The soil–foundation interface is discretized with 30 2.5D boundary elements, while 30×30 square quadrilateral boundary elements are used in the 3D validation calculations. This corresponds to nine elements per shear wavelength in the top layer at 100 Hz. As the rigid body translation of a longitudinally invariant structure is entirely two–dimensional (2D) and corresponds to plane strain conditions [1], the 2.5D calculation is restricted to $\bar{k}_y = 0$.

Figure 16 shows the real part of the vertical displacement $\hat{u}_z(\mathbf{x}, \omega)$ of the foundation and the soil at 25 Hz and 100 Hz. Results obtained with the 2.5D BE model (which represents an infinitely long rigid foundation), the 2.5D BE model with spatial windowing, and the 3D $\mathscr{H}$-BE model are compared. The 2.5D model is unable to account for variations in the longitudinal direction, as it is restricted to $\bar{k}_y = 0$ and thus purely 2D; the displacements consequently strongly differ from the 3D results at both frequencies under concern. Application of the spatial windowing technique distributes the energy over the entire wavenumber domain, which enables the correct representation of the variation of the wavefield in the longitudinal direction. This

leads to a very good agreement with the 3D calculations. The response of the foundation is also affected, however, and does not longer correspond to a uniform vertical translation.

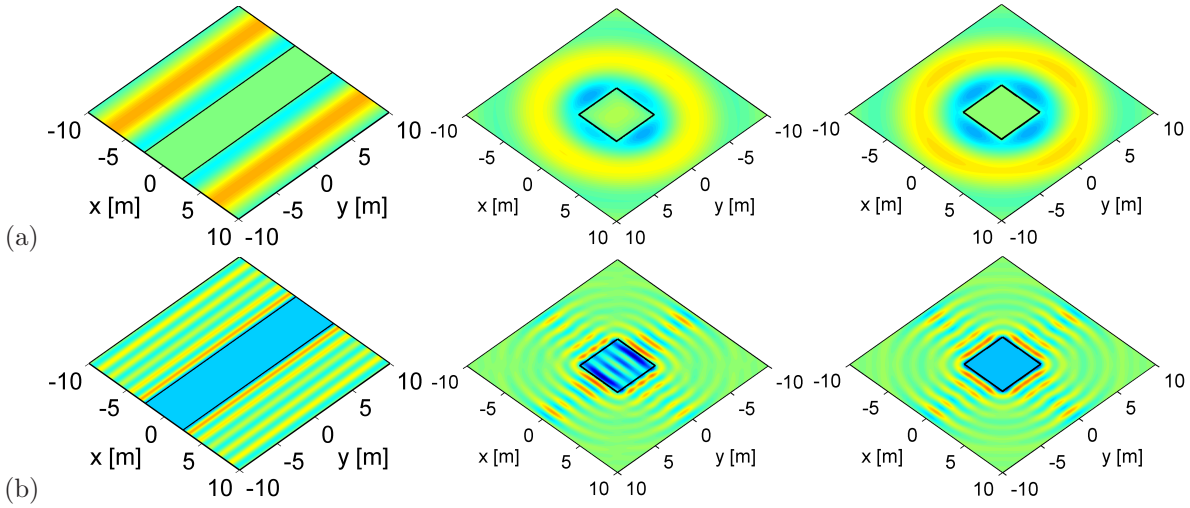

Figure 16: Real part of the vertical displacement $\hat{u}_z(\mathbf{x},\omega)$ of the foundation and the soil for a rigid surface foundation on a layered halfspace excited at its center by a unit harmonic vertical point load at (a) 25 Hz and (b) 100 Hz. The results are calculated by means of a 2.5D BE model (left), a 2.5D BE model with spatial windowing (middle), and a 3D $\mathscr{H}$-BE model (right).

The three numerical methodologies are furthermore compared in figure 17, which shows the free field mobility along the line $y = 0$ m at several distances from the foundation in the frequency range between 0 Hz and 100 Hz. As can be expected, there is a significant deviation between the 2.5D and 3D mobilities; the assumption of longitudinal invariance generally results in an overestimation of the free field mobility, especially in the far field. A very good agreement is achieved between the 2.5D model with spatial windowing and the 3D model, although some discrepancies arise in the near field. Figures 16 and 17 illustrate the appropriateness of the proposed methodology, even if applied to a short structure which is not quasi translationally invariant. The actual dimensions of the structure are not important; the spatial windowing technique is effective as long as the response is not dominated by the modal behaviour of the structure.

5.2. Flexible surface foundation on a horizontally layered halfspace

In order to account for the flexibility of the foundation, the structure is discretized with Kirchhoff plate elements which are coupled to the boundary elements on the soil–foundation interface. Within the frequency range of interest, the free foundation has natural frequencies at 24 Hz, 35 Hz, 40 Hz, and 62 Hz; only the modes at 40 Hz and 62 Hz can be excited by the loading under concern, however, as the projection of the excitation force on the other mode shapes equals zero.

Figure 18 shows the real part of the vertical displacement $\hat{u}_z(\mathbf{x},\omega)$ of the foundation and the soil at 25 Hz and 100 Hz. Results obtained with the 2.5D FE–BE model (for an infinitely long flexible foundation), the 2.5D FE–BE model with spatial windowing, and the 3D FE–$\mathscr{H}$-BE model are compared. At 25 Hz, a reasonable agreement between the results of the three models is observed, as the wavelength in the soil remains large compared to the dimensions of the foundation. At higher frequencies, however, the wavefield in the soil is more strongly affected by the presence of the foundation; a 2.5D calculation is unable to accurately represent the wavefield obtained with a 3D calculation. Application of the spatial windowing technique modifies the wavefield considerably, resulting in a much better agreement with the 3D calculations.

Figure 19 shows the free field mobility along the line $y = 0$ m at several distances from the foundation in the frequency range between 0 Hz and 100 Hz. Below 25 Hz, the three numerical methodologies yield the same result, as the wavelength in the soil remains large compared to the dimensions of the foundation.

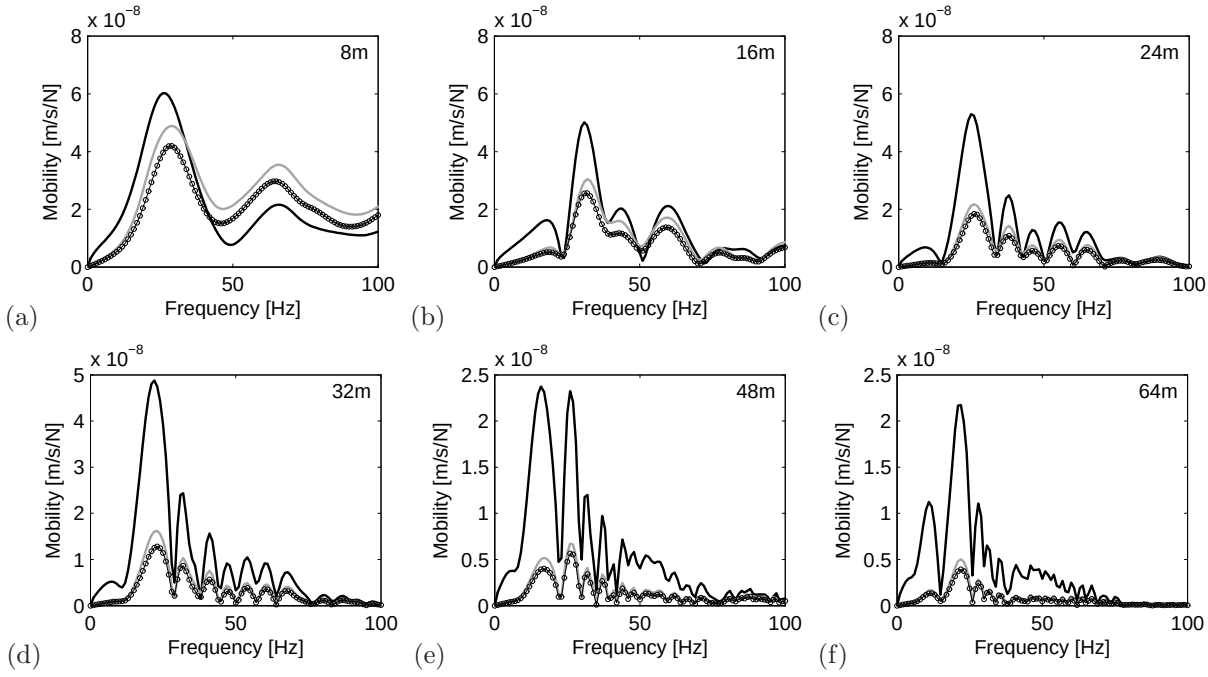

Figure 17: Free field mobility along the line $y = 0\,\mathrm{m}$ at (a) 8 m, (b) 16 m, (c) 24 m, (d) 32 m, (e) 48 m, and (f) 64 m from the center of a rigid surface foundation on a layered halfspace excited at its center by a unit harmonic vertical point load. The results are calculated by means of a 2.5D BE model (black line), a 2.5D BE model with spatial windowing (circles), and a 3D $\mathscr{H}$-BE model (grey line).

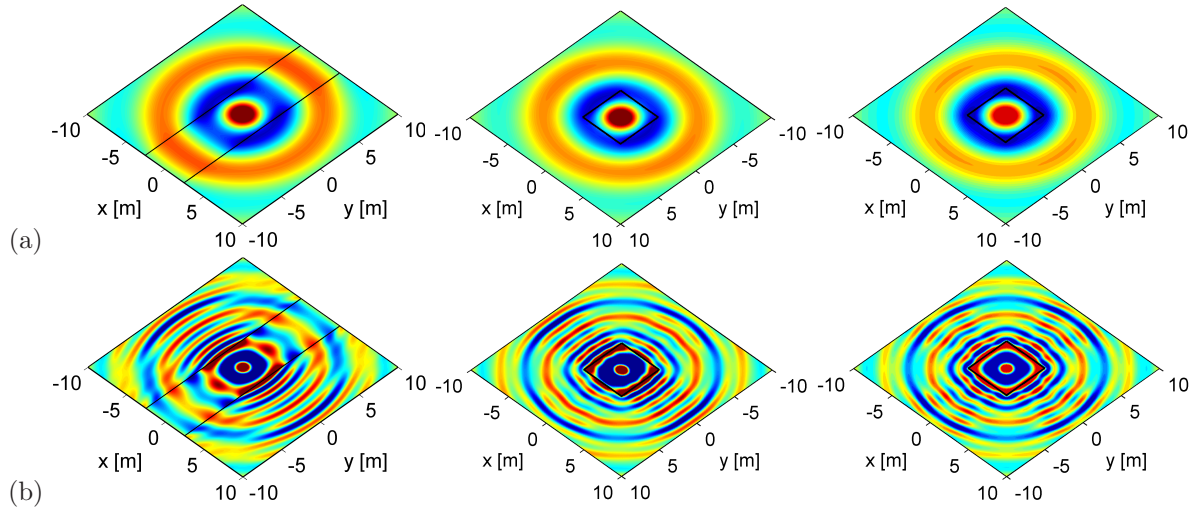

Figure 18: Real part of the vertical displacement $\hat{u}_z(\mathbf{x}, \omega)$ of the foundation and the soil for a flexible surface foundation on a layered halfspace excited at its center by a unit harmonic vertical point load at (a) 25 Hz and (b) 100 Hz. The results are calculated by means of a 2.5D FE–BE model (left), a 2.5D FE–BE model with spatial windowing (middle), and a 3D FE–$\mathscr{H}$-BE model (right).

Discrepancies between the 2.5D and 3D model are observed at higher frequencies, but these are much smaller than in the case of the rigid foundation considered in subsection 5.1. The deviations are more pronounced in the near field and are almost negligible in the far field. The mobilities obtained after application of spatial windowing are in much better correspondence with the 3D results, although the agreement at $x = 8\,\mathrm{m}$ remains relatively poor.

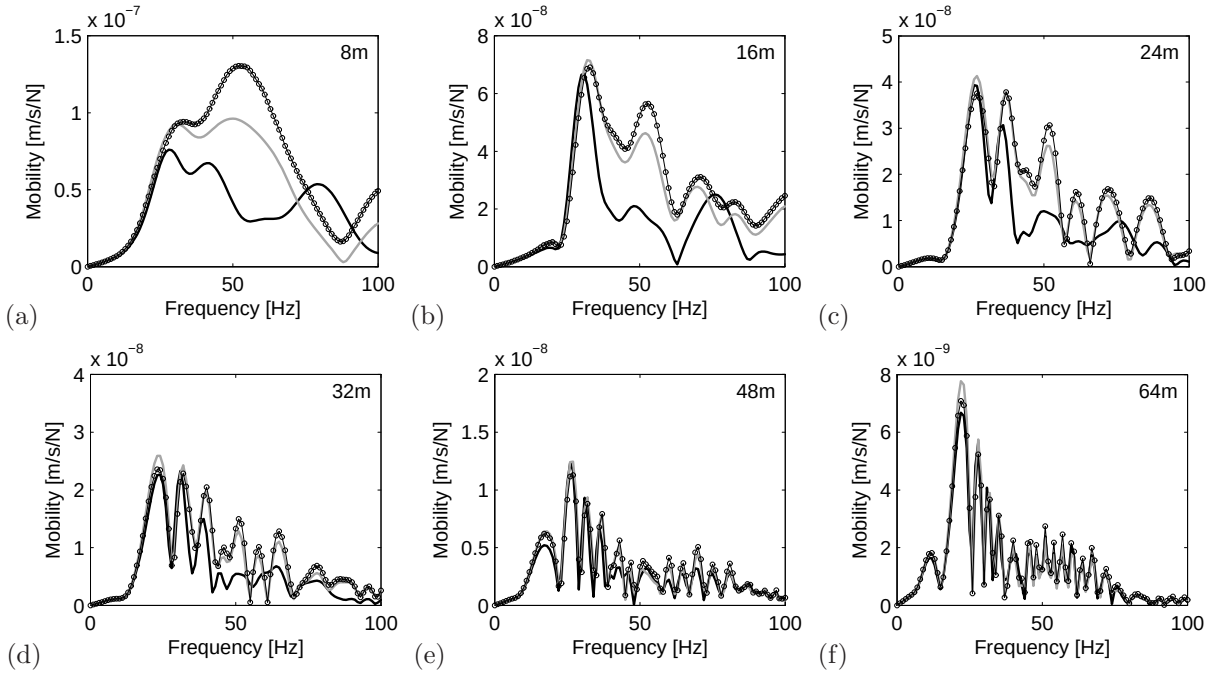

Figure 19: Free field mobility along the line $y = 0\,\mathrm{m}$ at (a) 8 m, (b) 16 m, (c) 24 m, (d) 32 m, (e) 48 m, and (f) 64 m from the center of a flexible surface foundation on a layered halfspace excited at its center by a unit harmonic vertical point load. The results are calculated by means of a 2.5D FE–BE model (black line), a 2.5D FE–BE model with spatial windowing (circles), and a 3D FE–$\mathscr{H}$-BE model (grey line).

The natural frequencies of the free foundation at 40 Hz and 62 Hz are not apparent in figure 19 due to the strong dynamic SSI and the associated radiation damping. This is also illustrated in figure 20, which shows the modulus and phase of the vertical displacement $\hat{u}_z(\omega)$ at the center of the foundation. The peak at 20 Hz corresponds to resonance of the foundation on the layered halfspace; it is not a natural frequency of the foundation. The response is thus not dominated by the modal behaviour of the foundation, explaining the suitability of the spatial windowing technique in the case under concern.

5.3. Flexible surface foundation on a single layer on bedrock

In order to further explore the limitations of the spatial windowing technique, a case study is discussed in this subsection where the eigenmodes of the foundation prevail in the response of the 3D coupled soil–foundation system. The layered halfspace considered in subsections 5.1 and 5.2 is replaced by a single layer on bedrock, with the same wave velocities and material damping ratios as the top layer of the aforementioned halfspace. The layer thickness h, however, is set to 0.375 m, which results in a cut–on frequency of $C_\mathrm{s}/(4h) = 100\,\mathrm{Hz}$; the surface waves hence remain evanescent in the whole frequency range under concern. The soil's shear modulus $\mu = \rho C_\mathrm{s}^2$ is furthermore reduced by a factor of ten by decreasing the soil density ρ to $180\,\mathrm{kg/m^3}$ to achieve a considerable stiffness contrast between the soil and the structure.

Figure 21 compares the modulus and phase of the vertical displacement $\hat{u}_z(\omega)$ at the center of the foundation, calculated with the 2.5D FE–BE model (for an infinitely long flexible foundation), the 2.5D FE–BE model with spatial windowing, and the 3D FE–$\mathscr{H}$-BE model. As there are no propagative surface

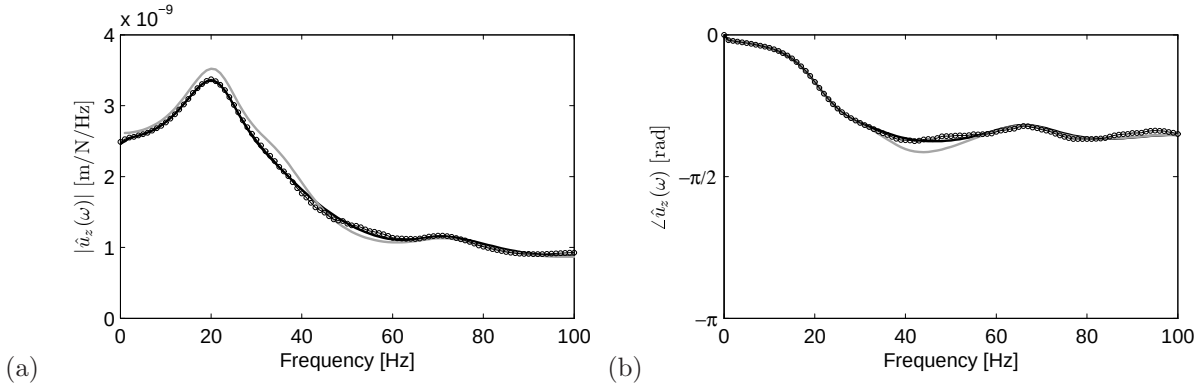

Figure 20: (a) Modulus and (b) phase of the vertical displacement $\hat{u}_z(\omega)$ at the center of a flexible surface foundation on a layered halfspace excited at its center by a unit harmonic vertical point load. The results are calculated by means of a 2.5D FE–BE model (black line), a 2.5D FE–BE model with spatial windowing (circles), and a 3D FE–$\mathscr{H}$-BE model (grey line).

waves in the soil, the radiation damping is very limited, and the eigenmodes of the foundation consequently prevail in the response of the 3D coupled soil–foundation system. The resonance peaks near 40 Hz and 62 Hz can clearly be distinguished in figure 21, which is also due to the low soil stiffness. The 2.5D approach gives a reasonable correspondence with these results below 40 Hz, but large discrepancies are observed at higher frequencies. Application of the spatial windowing technique does not lead to a better agreement with the 3D results, however. This example illustrates the shortcoming of the technique in case of low radiation damping in the soil, as it does not succeed to account for the dominant modal behaviour of the structure. It is emphasized that the prevalence of the structural modes is caused by the lack of radiation damping rather than the limited material damping in the soil. An increase of the latter results in a decrease of the peak values of $\hat{u}_z(\omega)$ but does not prevent the appearance of these resonances.

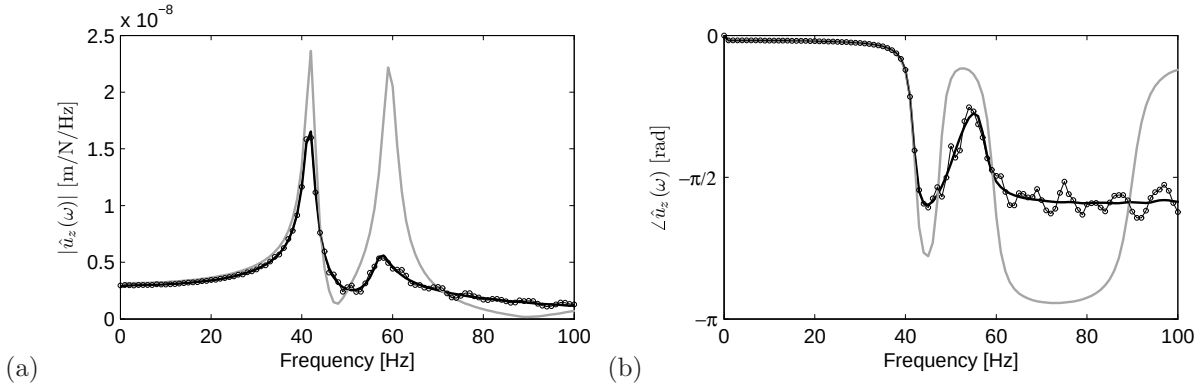

Figure 21: (a) Modulus and (b) phase of the vertical displacement $\hat{u}_z(\omega)$ at the center of a flexible surface foundation on a single layer on bedrock excited at its center by a unit harmonic vertical point load. The results are calculated by means of a 2.5D FE–BE model (black line), a 2.5D FE–BE model with spatial windowing (circles), and a 3D FE–$\mathscr{H}$-BE model (grey line).

6. Conclusions

In this paper, a spatial windowing technique has been presented that allows accounting for the effect of finite dimensions in 2.5D models for dynamic SSI. This technique enables the application of 2.5D models even if the assumption of longitudinal invariance is not fulfilled, hence maintaining the associated computational efficiency. The method redistributes the contribution of each wavenumber component over the

entire wavenumber domain and can as such be regarded as a postprocessing of the original 2.5D results. Spatial windowing only accounts for the diffraction occurring at the structure's extremities, however, and the existence of structural modes is not considered.

Numerical examples of elongated and short structures have been discussed to investigate the applicability of the proposed technique: an open trench as a vibration isolation screen, a stiff wave impeding barrier, a rigid and flexible surface foundation on a layered halfspace, and a flexible surface foundation on a single layer on bedrock. For each of these examples, full 3D calculations have been performed to provide a rigorous validation. It is demonstrated that the proposed technique is accurate as long as the modal behaviour of the structure does not dominate the response; the methodology is in that case even appropriate for short structures which are not quasi translationally invariant. The modal behaviour has only a limited influence in most of the applications due to the dynamic SSI and the associated radiation damping in the soil. If this is not the case, however, the spatial windowing technique reaches its limits of suitability.

Acknowledgements

The first author is a doctoral fellow and the third author is a postdoctoral fellow of the Research Foundation Flanders (FWO). The results presented in subsection 4.2 have been obtained within the frame of the EU FP7 project RIVAS (Railway Induced Vibration Abatement Solutions) [36] under grant agreement No. 265754. The financial support is gratefully acknowledged.

References

[1] S. François, M. Schevenels, G. Lombaert, P. Galvín, G. Degrande, A 2.5D coupled FE-BE methodology for the dynamic interaction between longitudinally invariant structures and a layered halfspace, Computer Methods in Applied Mechanics and Engineering 199 (23-24) (2010) 1536–1548.
[2] L. Gavrić, Finite element computation of dispersion properties of thin-walled waveguides, Journal of Sound and Vibration 173 (1) (1994) 113–124.
[3] L. Gavrić, Computation of propagative waves in free rail using finite element technique, Journal of Sound and Vibration 183 (3) (1995) 531–543.
[4] A. Stamos, D. Beskos, 3-D seismic response analysis of long lined tunnels in half-space, Soil Dynamics and Earthquake Engineering 15 (1996) 111–118.
[5] A. Tadeu, J. Antonio, E. Kausel, 3D scattering of waves by a cylindrical irregular cavity of infinite length in a homogeneous elastic medium, Computer Methods in Applied Mechanics and Engineering 191 (2002) 3015–3033.
[6] X. Sheng, C. Jones, D. Thompson, Modelling ground vibrations from railways using wavenumber finite- and boundary-element methods, Proceedings of the Royal Society A - Mathematical, Physical and Engineering Sciences 461 (2005) 2043–2070.
[7] L. Andersen, S. Nielsen, Reduction of ground vibration by means of barriers or soil improvement along a railway track, Soil Dynamics and Earthquake Engineering 25 (2005) 701–716.
[8] G. Lombaert, G. Degrande, D. Clouteau, Numerical modelling of free field traffic induced vibrations, Soil Dynamics and Earthquake Engineering 19 (7) (2000) 473–488.
[9] Y. Yang, H. Hung, A 2.5D finite-infinite element approach for modelling visco-elastic bodies subjected to moving loads, International Journal for Numerical Methods in Engineering 51 (2001) 1317–1336.
[10] Y. Yang, H. Hung, D. Chang, Train-induced wave propagation in layered soils using finite/infinite element simulation, Soil Dynamics and Earthquake Engineering 23 (2003) 263–278.
[11] S. François, M. Schevenels, G. Lombaert, G. Degrande, A 2.5D displacement based PML for elastodynamic wave propagation, International Journal for Numerical Methods in Engineering 90 (7) (2012) 819–837.
[12] S. Chaillat, M. Bonnet, J.-F. Semblat, A multi-level fast multipole BEM for 3-D elastodynamics in the frequency domain, Computer Methods in Applied Mechanics and Engineering 197 (49–50) (2008) 4233–4249.
[13] W. Hackbusch, A sparse matrix arithmetic based on $\mathscr{H}$-matrices. Part I: Introduction to $\mathscr{H}$-matrices, Computing 62 (2) (1999) 89–108.
[14] M. Villot, C. Guigou, L. Gagliardini, Predicting the acoustical radiation of finite size multi-layered structures by applying spatial windowing on infinite structures, Journal of Sound and Vibration 245 (3) (2001) 433–455.
[15] S. Ghinet, N. Atalla, The transmission loss of curved laminates and sandwich composite panels, Journal of the Acoustical Society of America 118 (2) (2005) 774–790.
[16] D. Rhazi, N. Atalla, Transfer matrix modeling of the vibroacoustic response of multi–materials structures under mechanical excitation, Journal of Sound and Vibration 329 (13) (2010) 2532–2546.
[17] J. Legault, A. Mejdi, N. Atalla, Vibro-acoustic response of orthogonally stiffened panels: the effects of finite dimensions, Journal of Sound and Vibration 330 (24) (2011) 5928–5948.

[18] D. Aubry, D. Clouteau, A subdomain approach to dynamic soil-structure interaction, in: V. Davidovici, R. Clough (Eds.), Recent advances in Earthquake Engineering and Structural Dynamics, Ouest Editions/AFPS, Nantes, 1992, pp. 251–272.
[19] D. Aubry, D. Clouteau, G. Bonnet, Modelling of wave propagation due to fixed or mobile dynamic sources, in: N. Chouw, G. Schmid (Eds.), Workshop Wave '94, Wave propagation and Reduction of Vibrations, Ruhr Universität Bochum, Germany, 1994, pp. 109–121.
[20] O. Von Estorff, E. Kausel, Coupling of boundary and finite elements for soil-structure interaction, Earthquake Engineering and Structural Dynamics 18 (1989) 1065–1075.
[21] P. Coulier, S. François, G. Lombaert, G. Degrande, Application of hierarchical matrices to boundary element methods for elastodynamics based on Green's functions for a horizontally layered halfspace, Engineering Analysis with Boundary Elements 37 (12) (2013) 1745–1758.
[22] L. Grasedyck, W. Hackbusch, Construction and arithmetics of $\mathscr{H}$-matrices, Computing 70 (2003) 295–334.
[23] M. Bebendorf, Hierarchical Matrices: A Means to Efficiently Solve Elliptic Boundary Value Problems, 1st Edition, Springer Publishing Company, 2008.
[24] P. Coulier, S. François, G. Lombaert, G. Degrande, Coupled finite element – hierarchical boundary element methods for dynamic soil–structure interaction in the frequency domain, International Journal for Numerical Methods in Engineering.
[25] Z. Ozdemir, P. Coulier, M. Lak, S. François, G. Lombaert, G. Degrande, Numerical evaluation of the dynamic response of pipelines to vibrations induced by the operation of a pavement breaker, Soil Dynamics and Earthquake Engineering 44 (2013) 153–167.
[26] L. Filon, On a quadrature formula for trigonometric integrals, Proceedings of the Royal Society of Edinburgh 49 (1929) 38–47.
[27] R. Woods, Screening of surface waves in soils, Journal of the Soil Mechanics and Foundation Division, Proceedings of the ASCE 94 (SM4) (1968) 951–979.
[28] S. Ahmad, T. Al-Hussaini, Simplified design for vibration screening by open and in-filled trenches, Journal of Geotechnical Engineering, Proceedings of the ASCE 117 (1) (1991) 67–88.
[29] H. Hung, Y. Yang, D. Chang, Wave barriers for reduction of train-induced vibrations in soils, Journal of Geotechnical Engineering, Proceedings of the ASCE 130 (12) (2004) 1283–1291.
[30] S. François, M. Schevenels, B. Thyssen, J. Borgions, G. Degrande, Design and efficiency of a vibration isolating screen in the soil, Soil Dynamics and Earthquake Engineering 39 (2012) 113–127.
[31] P. Banerjee, S. Ahmad, K. Chen, Advanced application of BEM to wave barriers in multi-layered three-dimensional soil media, Earthquake Engineering and Structural Dynamics 16 (1988) 1041–1060.
[32] The MathWorks, MATLAB Parallel Computing Toolbox User's Guide (2013).
[33] P. Coulier, S. François, G. Degrande, G. Lombaert, Subgrade stiffening next to the track as a wave impeding barrier for railway induced vibrations, Soil Dynamics and Earthquake Engineering 48 (2013) 119–131.
[34] F. Fahy, P. Gardonio, Sound and Structural Vibration: Radiation, Transmission and Response, 2nd Edition, Academic Press, Oxford, 2007.
[35] P. Hagedorn, A. DasGupta, Vibrations and Waves in Continuous Mechanical Systems, John Wiley & Sons, Chichester, United Kingdom, 2007.
[36] http://www.rivas-project.eu (2011).